I hereby declare that, except where specifically indicated, the work submitted herein is my own original work.

Hayden Taylor
26 May 2004

Acknowledgements

I am very grateful to everyone who has helped me during the year, particularly my supervisor, David Moore; research associates Mohamed Boutchich and Billy Boyle; my colleagues Johnny He, Sheridan Kates, Graham McShane, Rob Wylie and Richard Breen; Andrew Flewitt; Bernhard Klimt and Thomas Herrmann at Lumera Laser; Alan Heaver; Cinzia Casiraghi; Curran William; Fabrice Piazza; Simon Guest; Jack Luo; Simon Keighley; Jacques Boppe; Dave Lowrie and Sylvia Outerridge at IMAPS-UK; Benedetto Vigna at STMicroelectronics; Richard Syms at Imperial College; Neil Laurence; Mick Furber; Alistair Ross.

Links

Raw data, Matlab scripts, schedules of work and a log of samples processed may be seen at www2.eng.cam.ac.uk/~hkt21/yr4_project.

Contents

Figures

Tables

Abstract

This report presents:

- *recommendations for the effective laser ablation of thin films;*
- *work developing a simple method for determining Young's modulus of any thin film;*
- *results of the fabrication and testing of out-of-plane electrothermal MEMS actuators;*
- *the design of a bistable mechanism to hold MEMS optical components.*

Optical micro-electro-mechanical systems (MOEMS) demand a cost-effective way of holding sub-millimetre lenses, mirrors and fibres in place with sub-micron accuracy. Achieving such precise positioning *on-chip*, rather than by external manipulation, is the key to cutting costs. The race is therefore on to innovate in the field of MOEMS packaging. Two important aids to the rapid development of new materials for MOEMS packaging are the efficient and damage-free laser patterning of thin films and knowledge of the elastic moduli of these films. This report presents the results of characterisation work in those areas and of applying the findings to make prototypes of packaging structures.

Laser ablation is recognised as an attractive way of making prototypes rapidly at the microscale, but little work has previously been done to characterise the interaction of laser beams with thin films deposited on silicon substrates. Choosing appropriate ablation parameters is particularly important for brittle films such as silicon nitride because any microcracks introduced by the process may promote fracture. A test procedure has been devised whereby an array of lines is ablated in a film to be characterised. The laser's areal energy density, per pulse and in total, is varied, respectively, from column to column and from row to row in the array. Then the quality of the resulting cuts is inspected with optical microscopy, surface profilometry, and, in certain cases, scanning electron microscopy.

It emerges that the wavelength of laser light used and the laser's per-pulse areal energy density, or *fluence*, are the key parameters. It is preferable to choose a wavelength at which the film absorbs strongly and does not transmit: in this way, ablation of the substrate, and hence damaging explosions beneath the film, are avoided. In the cases of silicon nitride, silicon carbide, diamond-like carbon and photoresist, bands of fluences have been observed within which the films are completely removed and yet the substrate is not significantly ablated. This strong selectivity may be applied to the prototyping of smooth-walled microfluidic channels. The main limitation of the nanosecond-pulse ablation system investigated is its cutting speed, which is slow in comparison with shorter-pulse length lasers or conventional reactive ion etching of established designs.

The successful mechanical design of MEMS often relies on knowing the **elastic moduli** of the materials used. Existing test methods are either laborious or insufficiently

accurate. The method presented here involves simply scanning a stylus profilometer from the root to the tip of a cantilever microbeam fabricated in the film to be tested. A trace of the stylus's horizontal position against its vertical displacement is obtained, and the trace's shape is interpreted to give an estimate of Young's modulus. We expect that the cubic term in the position–displacement trace will be unaffected by any fabrication imperfections. A test site has been designed comprising 20 microbeams that can easily be laser-micromachined on a 5mm square sample.

The test site has been fabricated in SiN and the results interpreted using each of five candidate analysis routines. The consistency of results is limited. It emerges that two factors contribute significantly to uncertainty in the extracted modulus: noise in the trace from vibration and residual dirt, and deviations of the actual beam deflections from a simple linear model of a bending cantilever. It is believed that those analysis routines that rely on fitting a third-order polynomial to the position–displacement data are highly susceptible to errors caused by noise in the trace. Meanwhile, a routine that involves simply fitting a straight line to the cube roots of the stylus displacements is less affected by noise but gives an answer that is inevitably biased by root under-cutting, sample tilt, and any initial curvature (curling) of the film. The smallest uncertainty obtained is of order 15%, and work is continuing to reduce that figure.

Moving on to exploit this characterisation work, laser micromachining has been used to fabricate a set of electrothermally actuated, U-shaped, metal-on-SiN **bi-layer beams**. The beams' actuated curvatures have been measured as a function of the input electrical power. It remains now to combine electrothermally actuated curvature with the large elastic deflections necessary for the beams to function as clips holding MOEMS components. Simulations of the existing structures (effected using spreadsheet software and a novel energy minimisation procedure) suggest that the clips' required bending stresses would far exceed their tensile strengths when deflected enough to provide an adequate holding force. The design of microclips is discussed in some detail, and ways are proposed of improving the choice of materials. Initial investigations of two alternative packaging concepts are presented: a bistable mechanism that folds out of the plane of a chip, fabricated by deep reactive ion etching of bulk silicon, and inflatable microclips made by welding polythene films together.

In summary, test procedures have been developed to characterise the laser ablation of MEMS thin films and to determine Young's moduli of those films. These procedures have been carried out to provide information about a set of typical films. Laser ablation has been employed to process a set of bi-layer microclips, which have been tested.

1. Introduction

The telecommunications industry is clamouring for improvements in the reliability and cost of optical microsystems (MOEMS), which, by shrinking optics to the sub-millimetre scale, offer superior performance for products such as cross-connects, (de)multiplexers and attenuators. Compared to conventional electronic cross-connects, MOEMS solutions offer data rates and port counts up to 100 times greater [Bishop].

An example of a MOEMS system, an optical demultiplexer, is shown in Figure 1 [Moore2]. Several wavelengths of light within a fibre carry different streams of data and need to be separated before detection. When manipulating the necessary mirrors, lenses and filters during manufacturing, precision is vital to minimise coupling losses during use [Gambling]. That precision is often achieved with external *nanomanipulators*, which position components on the optical 'bench' before they are glued in place. Because each component is manipulated in turn and nanomanipulators are expensive, MOEMS devices remain costly. Indeed, [Culpepper] attributes 50% of the packaging costs of MOEMS to the expense of nanomanipulators.

Figure 1: MOEMS optical demultiplexer; Table 1: Abstraction of MOEMS requirements

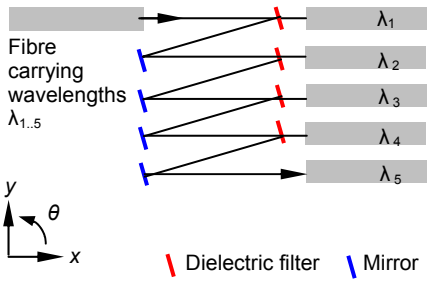

		Angular degrees of freedom			
		0	1	2⁺	3
Linear DoF	0	filter			
	1*			plane mirror	diffraction grating
	2			detector§	triangular prism#
	3	spherical lens		parabolic lens or mirror; emitter	

θ, x, y: in plane
z, φ, ψ: out of plane

* *x* or *y*
⁺ includes *θ* plus *φ* or *ψ*
§ translation in *x* or *y*, plus *z*
# positioning in *x* and *y*

Because precision and low cost are both crucial they find themselves in fierce competition. Prolific innovation has sought to reconcile the two requirements [Walker], and the results so far are summarised in Table 2 below. It shows that a common drive is to reduce MOEMS' costs by building component manipulation, and possibly some self-testing, into the devices themselves, avoiding the cost of a nanomanipulator and allowing many devices to assemble themselves simultaneously. Against these savings is the possible new cost of any added chip area.

If we consider the complexity of manipulation required to achieve good coupling to a variety of optical components, we obtain Table 1. The six possible degrees of freedom are never all required together, and where light passes between components sharing axes of rotation or translation, the design can be simplified. Out-of-plane motion is often vital. For a

0.1dB loss from fibre to fibre, the cumulative misalignment must be better than 0.7μm or 0.5˚ [Mickelson]. Component size tolerances are often much larger than the final required position accuracy: a typical reflector [Etalon] has a thickness of 500±50μm. This 'slop' must also be compensated for.

Table 2: Existing approaches to MOEMS packaging

Method	Pros	Cons	References
Position components on chip with nanomanipulator; glue in place	Precision ensured	Serial process, so slow; nanomanipulators cost >$50k each; component positions may drift in use if glue is not stable	[Culpepper]
Reduce cost of nanomanipulator through elegant mechanical design	More machines may be purchased (at $3k each), so throughput is increased at the assembly stage	There is still a limitation on the rate at which devices can be assembled	[Culpepper] ('HexFlex')
Surface-micromachined clips (silicon nitride) hold optical fibres into precisely machined V-grooves in silicon	Anisotropic etching of Si is exploited to provide kinematic location	Not appropriate for rectangular components with large dimensional tolerances	[Bostock]
Surface micromachining of several layers of polysilicon makes mechanisms which assemble out-of-plane when electrically actuated	Versatile: can achieve precision in several directions at once	Complex; expensive	[Sandia] ('Summit' process)
Released GaAs structures self-assemble out-of-plane owing to stress gradients introduced to selected regions by molecular beam epitaxy.	Very precise and versatile motion when characterised	Extremely expensive; so not suitable for mass production; only small forces can be supported	[Kubota]
Use deep reactive ion etching of silicon-on-insulator to make an in-plane moving stage	Stage can support a relatively large load; clever design of locking teeth sets gives high resolution	Only in-plane motion is possible; adding a second degree of freedom will increase complexity greatly	[Enzler]
Exploit surface tension of molten solder beads to pull surface-micromachined components (e.g. lenses) out-of-plane	Requires fewer layers than the Summit process, so likely to be less expensive	Much effort required to design surface tension assembly process for new structures	[Syms1]
Build components into the microsystem at the processing stage instead of adding them later. Use flat components where possible e.g. Fresnel lenses. Metallise layers for mirrors.	Can use the precision of photolithography; assembly time cut	Built-in components may not perform as well as separate ones. (e.g. mirrors need etch holes, leading to diffraction [Zou])	Mirrors (corner-cube reflectors): [Chu] Thermal reflow of polymers for lenses: [Yang]

It is evident that the use of thin films in MOEMS packaging has not been extensive, and this is an area that warrants further investigation. The simplicity of processing thin films is surely worth consideration, given that we are seeking to make MOEMS packaging cheap to mass-produce.

This report starts with work that explores ways of mechanically characterising thin films for MEMS and ablating them with a laser to make prototypes rapidly. The insights gained from that work feed into the investigation of three new MOEMS packaging concepts, each focussing on achieving manipulation out of the plane of an optical bench. Each concept is aiming to provide precision at lower cost than has previously been achieved.

Work on each section of the project has developed along separate lines, and so detailed introductions and conclusions are presented separately for each part. The work on extracting Young's modulus of thin films — a problem of great interest to the MEMS community — has expanded to take precedence over some of the work on applications.

It is not just for *optical* microsystems that thin film characterisation and laser micromachining are of interest. For example, MEMS packaging that made electrical connections would be valuable: compared to wire bonding, it could reduce the parasitic inductances between integrated circuit dies in a system [Oshima]. The project's early sections are kept as general as possible so as not to exclude such possibilities.

2. Characterisation of laser micromachining

Because the mechanical design of MOEMS packaging devices is difficult, it is likely that we will need to cycle quickly through a series of physical prototypes. For a design based on thin films, laser micromachining is an attractive way of making rapid prototypes. One promising approach [Moore1] is illustrated in Figure 2: a laser directs a stream of focussed pulses at a thin film or sandwich of films that has been deposited on a substrate (typically silicon). The thin films are heated by the incident light, evaporate, and leave the substrate exposed. The material is moved under computer control to define a design in the film. A straightforward etch of the substrate releases structures made from the film(s).

The particular system under consideration [NewWave] uses a frequency-doubled or -tripled YAG laser, delivering pulses at 532nm or 355nm each containing up to 0.6mJ and lasting about 3ns. The spot is shuttered to a rectangular beam with maximum dimensions ~60μm square, at which all of the 0.6mJ may be transmitted to the material. Pulses can be delivered at 1–50Hz and the sample can be moved with micron precision (although not always repeatably) and at speeds of order 0.1mm.s^{-1}. This section describes work to

characterise the system's performance on a range of typical MEMS materials, and develops guidelines that inform, for example, the processing of the bimorph clips in Section 5.

Figure 2: laser micromachining of thin films

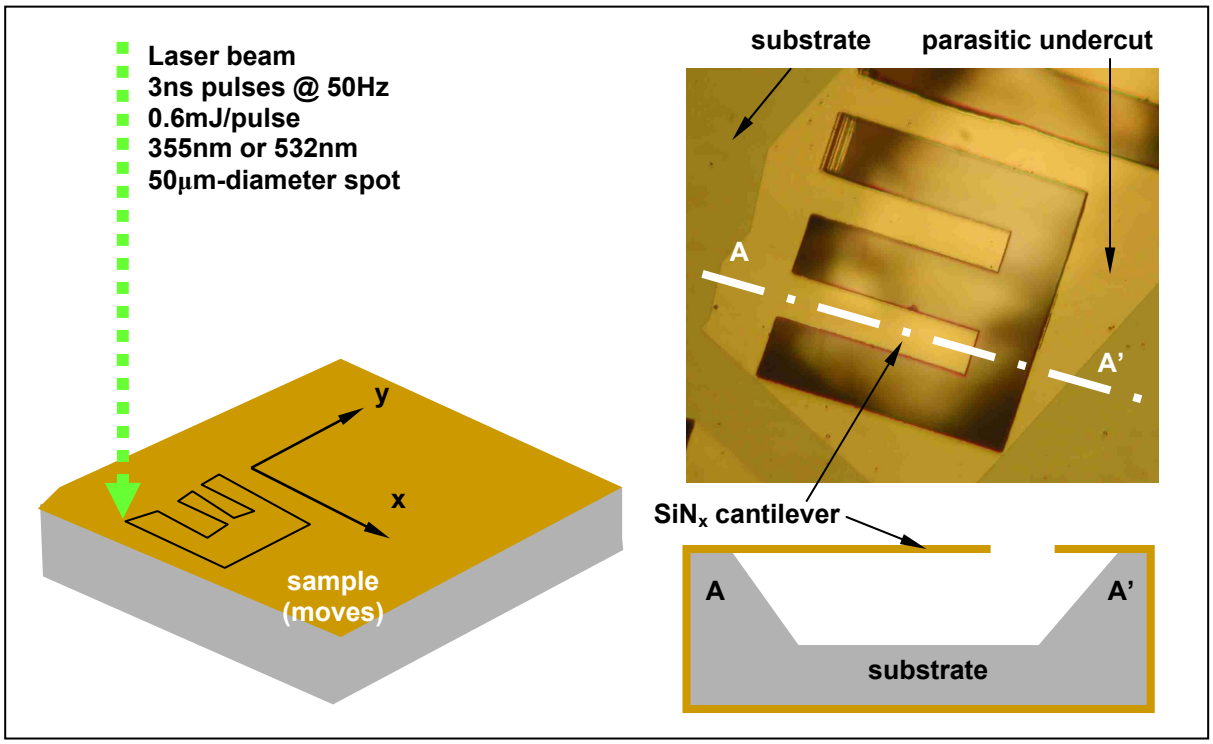

Previous work

The merits of laser micromachining are well documented: the procedure is rapid; the process is insensitive to grain orientation; it is even possible to produce arbitrary three-dimensional structures by stereolithography. For a project such as this, where we are investigating a large range of materials, the cost in time of implementing chemical etches for all those materials would be too great, and laser micromachining is especially valuable. Lasers have been used for drilling and cleaning at the microscale [Meijer], for repairing MEMS structures suffering from stiction [Rogers], and for the manipulation and assembly of MEMS [Holmes]. Although the process's spatial resolution remains inferior to that of reactive ion etching, its main competitor in thin-film processing, efforts are being made to improve the quality of finish provided by lasers: shortening pulses to picosecond or femtosecond lengths ([Dong], [Lumera]) is believed to cause less thermal damage to films.

Work modelling the physics of laser ablation has concentrated mainly on the *deposition* of thin films [Singh]. In the micromachining field, however, [Jackson] relates ablation depth per pulse to fluence (incident energy density per pulse), [Hogan] gives results for the ablation rates of spun-on glass, and [Silverstein] reports the use of a laser to polymerise a gas on to a substrate, forming patterns without creating debris. A comprehensive

comparison of the laser machining properties of typical MEMS materials is yet to be made, however.

Experimental design, results and discussion

Silicon nitride is of interest as a MEMS material because of its ease of deposition with limited residual stress, and its stiffness. Knowing how to pattern it well is vital. Because SiN is a rather brittle material, it needs to be kept free of unnecessary cracks: the critical crack length above which failure in SiN would be by fracture rather than yielding is estimated at about 20μm, of the same order as the laser beam size. Finding parameters that limit film damage is crucial.

Figure 3: comparison of different wavelengths for patterning SiN

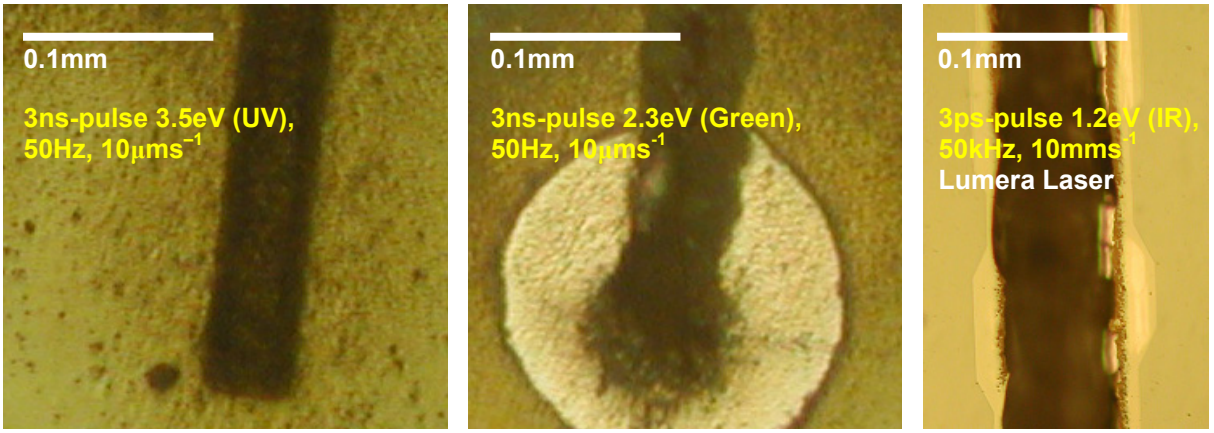

Figure 3 shows the effects of three wavelengths of radiation on identical samples of 2.4μm-thick Si-rich SiN_x/Si (from Twente Microproducts, or 'TM', a company which no longer trades). It is clear that the UV radiation gives the cleanest cut, whereas the green seems to have penetrated the nitride and ablated the silicon substrate, pushing debris up through the film, delaminating and chipping it. The sample on the right was machined by me with IR radiation from a ps-pulse laser at Lumera Laser, Kaiserslautern. Both wavelength and pulse duration differ between this sample and those from our ns-pulse machine, so a direct comparison is not possible, but the film appears to have been badly chipped at the edges. We gain some support for the idea that longer wavelengths ablate the substrate in addition to the film when we consider the transmission spectrum of the material, shown in Figure 4. At UV, almost nothing is transmitted and the radiation must be absorbed or reflected by the film. At green, about 15% is transmitted, and that appears to be enough to cause the explosion of the substrate that was observed. The absorptivity spectrum of ta-C (diamond-like carbon), another thin film of interest in MEMS, shows a similar behaviour: it is more absorbent at UV, and so should probably also be processed at UV.

Figure 4: (a) Transmission spectrum of SiN (TM type) [courtesy M Boutchich, CUED] and (b) Absorptivity spectrum of ta-C [courtesy F Piazza, CUED]

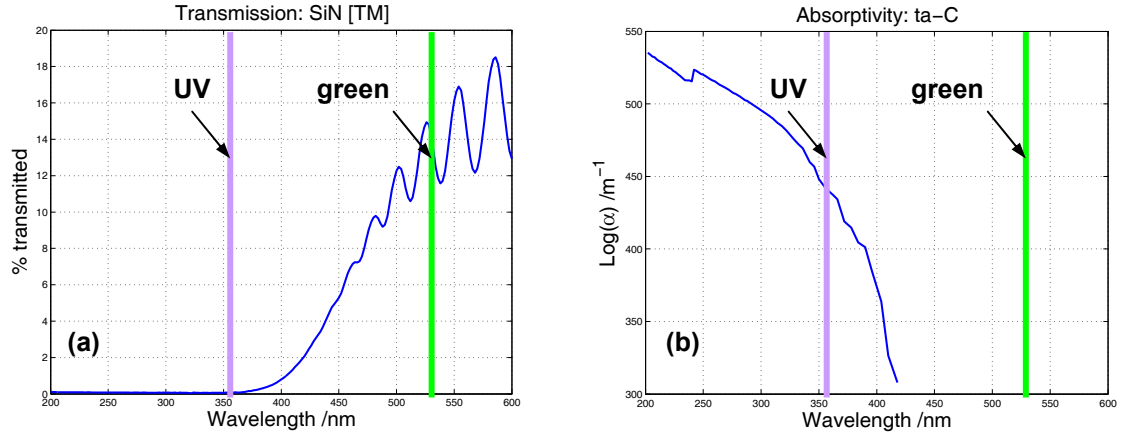

We now want to consider the exact impact of laser parameters on the quality of the cut obtained. A test has been devised for this work in which an array of lines (Figure 6(b)) is ablated on any film to be characterised: each of the 22 columns of lines has constant pulse fluence and each of the 5 rows has constant total incident energy density. The total energy density is kept constant along the rows by increasing the beam speed proportionally with pulse fluence, while the pulse rate remains constant at 50Hz. This ensures that the correct number of pulses strikes each point on the film. Nine thin films were tested and the results are collated in Figure 5 below. The beam size was ~57μm square. SiN, ta-C, bare silicon and AZ5214 resist were tested with UV radiation while the metals and silicon-on-insulator were subjected to green light and SiC was tested with both wavelengths.

The upper plot in Figure 5 was obtained not from the array of lines but by manually applying series of pulses to the films and observing how many pulses were needed at each fluence to penetrate through the top film to the substrate. Because the laser system directs the beam through the objective of a microscope it is possible to inspect the film surface optically between pulses. The metals and SOI are omitted from this graph because there was no clear point at which the film had been removed but the substrate was intact. Surprisingly, the Nortel-supplied SiN required more pulses at a given energy to be penetrated than the thicker TM SiN. It is possible that the thickness of the Nortel nitride happened to be such that there was constructive interference between the components of light reflected from the top and bottom of the film, and thus that its reflectivity was high, reducing ablation efficiency. The exposed material seemed to be removed progressively in 'patches' from the substrate, so the film thickness at any given point was probably constant until removed. The ta-C film required still more pulses for a given fluence in spite of being even thinner: the material's extremely high melting and boiling points probably explain this. SiC behaved like the SiN[Nortel] at

higher fluences but was not ablated at all below about 4.5 . 10^4 Jm^{-2} per pulse. The photoresist has a much lower boiling point and, hence, was much more easily ablated.

Figure 5: Laser micromachining results for the nine thin films tested

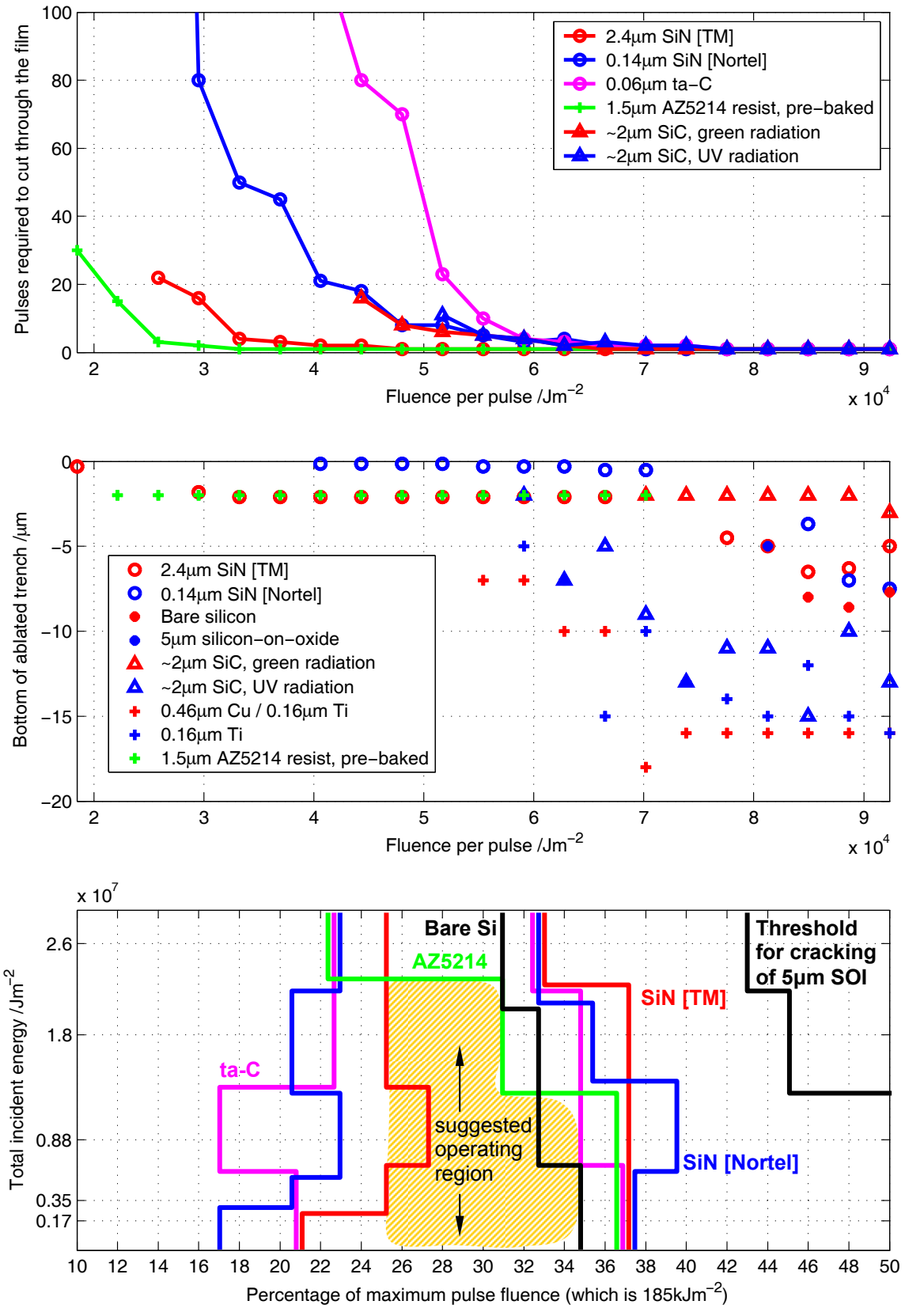

The middle graph in Figure 5 plots measured ablated depths against fluence for a total energy density of $1.8 \cdot 10^7$ Jm^{-2}. The values were obtained by scanning a stylus profilometer along the second row of the ablation grid. As the typical trace in Figure 6(a) hints, any debris surrounding the lines caused significant vibration of the stylus and made traces difficult to interpret. Hence much of the data for larger depths should be taken to have an uncertainty of about ±50%. The significance of the plot is that, for SiC ablated with green radiation, SiN, and AZ5214 resist, there is a range of pulse fluences within which the film appears to be completely ablated while the substrate is not significantly affected. The runs of data points at depths equal to the film thicknesses provide the evidence. This is a surprising result when we consider that the melting points of SiC (~2650˚C), ta-C (>4000˚C) and SiN (~1900˚C) are much larger than that of Si (1410˚C). We might therefore expect the Si substrate to vaporise at lower temperatures than the films; yet we have observed the film being ablated exactly as far as the silicon surface, and no further.

A suitable explanation for this phenomenon may be that offered by [Dong] in the context of the machining of 3C–SiC using a fs-pulse laser. It was found that, using fs-pulse fluences between about $1 \cdot 10^4$ and $2 \cdot 10^4$ Jm^{-2}, ablation was 'defect-activated': the material apparently became polycrystalline and grain boundaries then vaporised. Our SiN, SiC and ta-C will contain defects, while the Si substrate is processed to be relatively defect-free; hence the observed high selectivity of the ablation process at fluences up to $9 \cdot 10^4$ Jm^{-2} could well point to the significance of defects in the film.

Figure 6: (a) Typical profilometer trace used to determine ablation depth as a function of pulse fluence; (b) Part of optical micrograph of ablation test grid (SiN[Nortel])

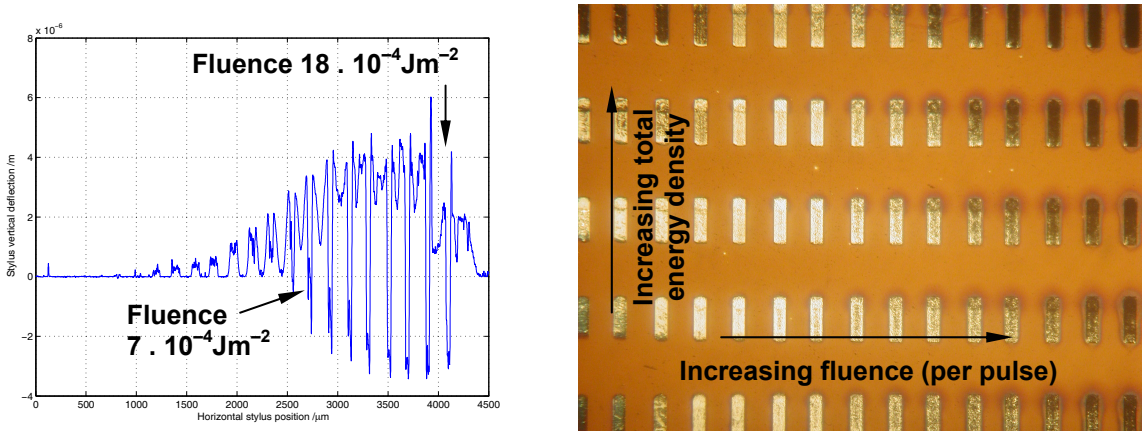

The Cu coating seems to have promoted the rate of ablation. A consistent series of trench depths greater than 15µm was measured for the higher fluences, while bare silicon at the same fluences was ablated by less than 10µm. It seems likely that the sputtered Cu surface absorbed more of the radiation than the bare Si, which was highly polished.

The lower plot in Figure 5 collates information from a third source: optical micrographs of the test grids such as that in Figure 6(b). Where the bottom of a trench is shiny, it is assumed that the film, but not the substrate, has been ablated. The lower-fluence boundary plotted for each material shows the threshold for complete ablation of the film; the upper boundary indicates the start of ablation of the substrate. There were no shiny regions for SiC/Si or Cu/Ti/Si, even though plateaux in the depth–fluence relationships were observed from profilometer data. In general the thresholds are rather insensitive to the total number of pulses seen by the material, implying that the thermal activity of each pulse is self-contained.

In the lower plot of Figure 5, all the upper boundaries compare well to that measured for the ablation of bare silicon, although that boundary itself is rather higher than the 3.5–4 . 10^4 Jm^{-2} reported by [Singh]. The difference here is perhaps because the surface tested in our experiments was highly polished, and would have reflected much of the radiation. That is not a complete explanation, though: performing the same test on the *un*polished side of a Si sample appeared to reduce the ablation threshold only by about 5%.

Scanning electron micrographs of SiN[TM]/Si ablated with three different fluences are shown in Figure 7: the earlier observations are confirmed, with complete, clean ablation of the SiN seen in (b) and melting and recasting of the Si in (c).

Figure 7: SEM cross-sections of SiN[TM]/Si ablated at three different per-pulse fluences and 0.9 . 10^4 Jm^{-2} total energy density

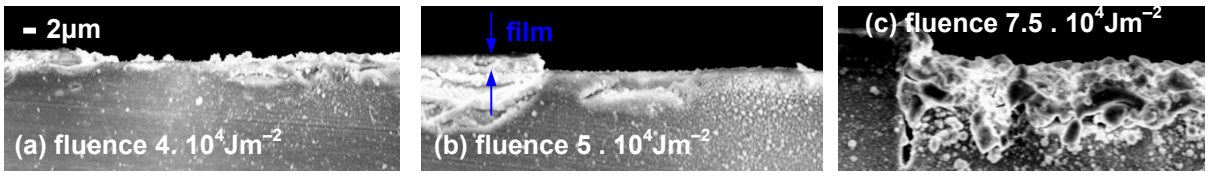

Also shown on the fluence–total energy density plot in Figure 5 is a threshold for damage to 5µm silicon-on-oxide. It was found that at high pulse fluences and total energy densities, there was severe cracking of the silicon layer. This cracking perhaps happened because stresses arising from the differential thermal expansion of the silicon and the oxide exceeded the strength of the silicon, or because, as the oxide started to be ablated, debris was pushed up and delaminated the silicon layer above.

We may also wish to **micromachine *bulk* silicon**, and results from the ablation of a sample of 65µm-thick silicon-on-oxide are shown in Figure 8. The laser system was programmed to focus the beam 12µm further down into the material with each pass of the beam. A cross section through some of the features ablated is shown in Figure 9. The ablation rate per pulse tails off as the ablated depth increases, probably for four reasons. Firstly, as the

laser strikes deeper in the material, heat conduction from the trench bottom becomes more three-dimensional and the peak temperature will reduce, meaning that less material is vaporised per pulse. Secondly, the walls of the trench begin to block the edges of the convergent, incident laser beam from reaching the target. Thirdly, as the trench gets deeper debris has more difficulty escaping from the cut and probably builds up in the trench, reducing the ablation rate. Fourthly, the location of the trench bottom gradually diverged from the position at which the beam was focussed (the red line in Figure 8). At 35–40 pulses, the green radiation appeared to cut significantly further. This could be because the laser system was not actually delivering the same power at the two wavelengths: the frequency-doubling crystal in the system may have operated more efficiently than the frequency-tripling one.

Figure 8: Ablated depth against number of passes for bulk silicon: fluence 1.9 . 10^5 Jm^{-2}, 50Hz, beam speed 25µms^{-1}

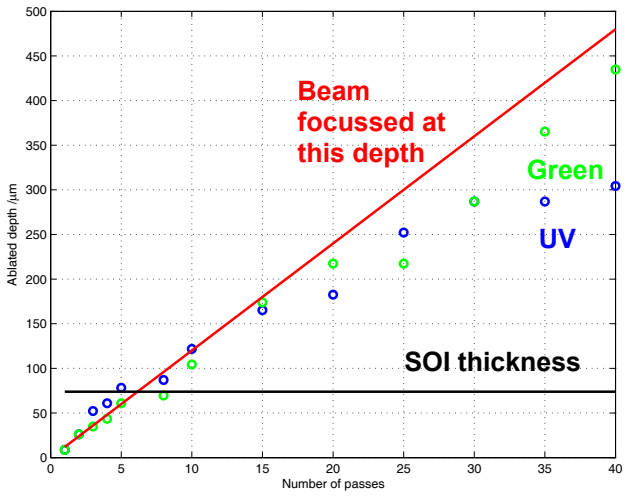

Figure 9: SEM cross-section of features ablated with green radiation

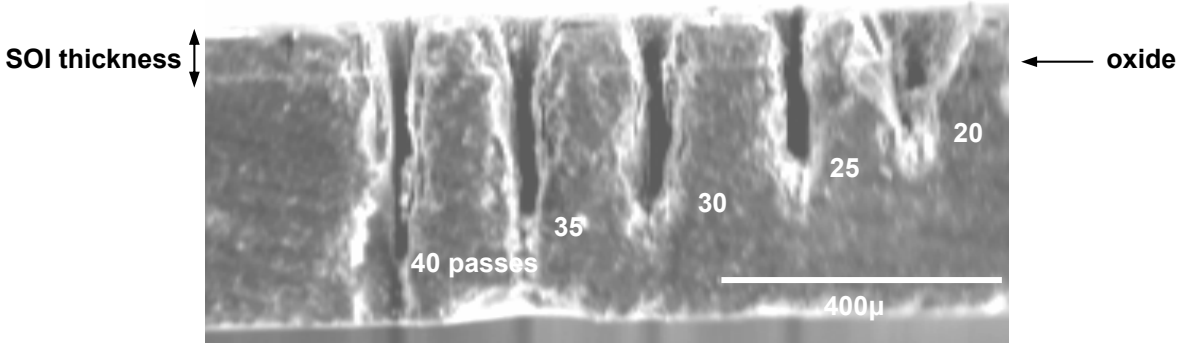

It is instructive to look at the **debris** created during the ablation of thin films. Figure 10 below shows four sequences of lines that were ablated in 0.14µm-thick SiN[Nortel]/Si. Each segment of the long continuous lines was ablated using different parameters. When increasing pulse rate in proportion with the beam speed (i.e. keeping the physical separation of consecutive pulses equal), the density of debris produced and its distance from the cut

remain almost constant, implying that the time between pulses is long enough that any two pulses can be treated as independent. If the speed is held constant while the pulse rate increases, or *vice versa*, the physical separation of consecutive pulses changes. Where consecutive pulses are closer together, debris looks denser and falls closer to the cut. When pulses are very close together, there is a characteristic band of light-coloured debris, probably Si, about 30µm from the cut. All the debris is loose or reactive enough that it disappears after a few minutes in KOH solution.

Figure 10: Experiments on the production of debris (the tick marks are ablated at arbitrary parameters)

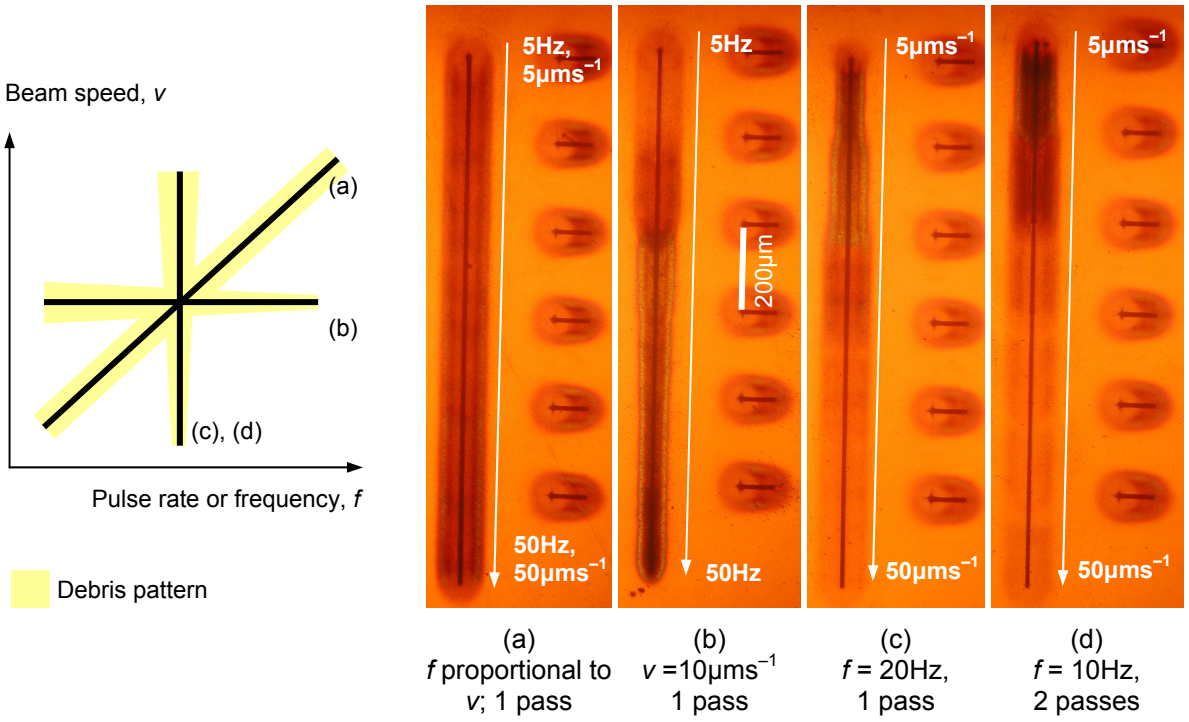

We gain support for the idea that the physical relationship between *consecutive* pulses is important by comparing lines (c) and (d) above: although the same number of pulses was used in total, the debris was more widely spread if the radiation was delivered in two passes.

Figure 11: Possible explanation of debris formation

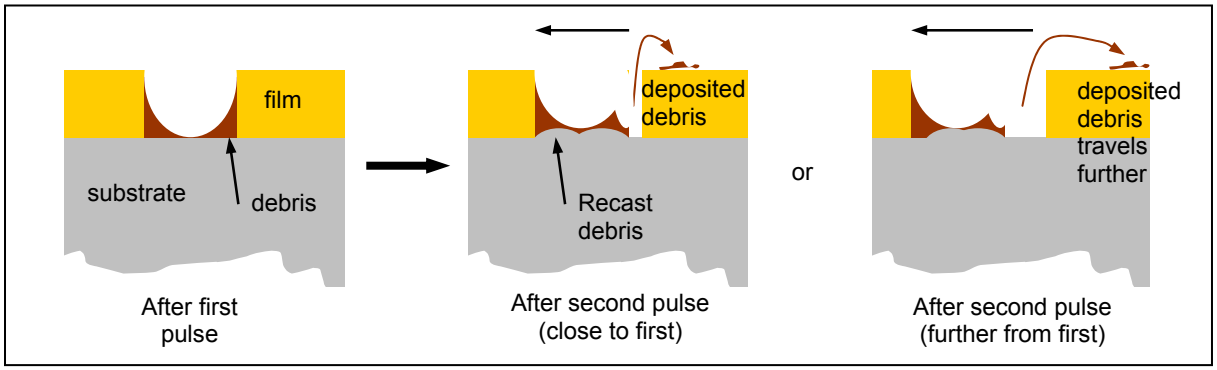

A possible explanation is illustrated in Figure 11. A laser pulse will heat the material it hits and may re-melt any debris from the previous pulse that is in the direct path of the beam. The expanding plasma brought about by the laser will push loose debris *next to* the beam out of the trench and on to the top of the film. If the distance between pulse centres increases, there is more loose debris to be ejected per pulse and we might well expect that to increase the likelihood of some of the debris travelling further.

Conclusions and future work

This work has identified suitable processing parameters for the ns-pulse laser ablation of typical MEMS materials. SiN, ta-C, and photoresist are cleanly ablated by UV radiation, while Si, SiC, Cu and Ti are ablated effectively by green, without obvious damage to the surrounding material. If SiN, ta-C or photoresist are on a Si substrate they can be ablated so as to remove the film but not the substrate. Typical pulse fluences that should be employed to achieve this effect are about 5–6 . 10^4 Jm^{-2}. This property could be useful for prototyping shallow microfluidic channels, where the roughness of the channel strongly governs the fluid flow.

If it is important, for any reason, to minimise the distance travelled by debris from a deep cut, this may be achieved by moving the beam slowly rather than by making several faster passes. It is possible to cut through silicon at least 400μm thick with a series of about 40 passes of green radiation at an energy density of about $20MJm^{-2}$ per pass. The trench made will not have perfectly vertical walls, however, and the ablation rate per pulse tends to reduce with depth.

The values of fluence and total energy density quoted in this section were calculated by assuming the system to be operating exactly as specified. Future work should seek to measure the fluence accurately, to reinforce comparisons with other work. An attempt should also be made to ablate metals and Si with UV light, to complete the comparison of the two wavelengths. If UV is not completely reflected by metals and can successfully ablate them, a 355nm laser would be conclusively more versatile than a 532nm one, because it would process a larger range of materials without damage. A more thorough comparison of the merits of fs-, ps-, and ns-pulse length ablation systems is also needed. One question to be asked during such a comparison is whether, with the shorter pulse lengths, any removed material is vaporised before a plasma has time to form above the cut.

3. Determining Young's modulus of thin films

In any MEMS design employing a thin film, knowledge of that film's mechanical properties, including the elastic modulus, *E*, is crucial. Central to the design of the bi-layer 'microclips' discussed in Section 5 is the ability to estimate the holding forces that they will offer when retaining optical components. Even more vitally, the design of a surface-micromachined accelerometer relies on the accurate determination of the spring constant of the proof mass's support flexures. The importance of measuring *E* has spawned an array of microtesting methods, which are summarised in Table 3 below:

Table 3: Evaluation of Young's modulus measurement methods

Method	Pros	Cons	References
Bulge: apply differential pressure across a membrane of the film under test and measure deflection	Widely adopted, so analysis well understood	Test apparatus complex; compliant banks of membranes will affect accuracy	[Tabata]
Hardness test: apply a nanoindenter to the film *on* its substrate	No special processing of test structures required	Difficult to decouple film's modulus from the compliance of the substrate	[Baker]
Use a **nanoindenter** to deflect a cantilever or bridge made from the film under test	Very precise measurement of force and deflection is possible	Measurement of nanoindenter position imprecise; imperfections in the manufacture of the test structures lead to large uncertainty in the modulus	[Weihs]
Measure the **resonance frequency** of a cantilever beam of the film	Simple test method	Imperfections at the cantilever root affect resonance frequency, as, perhaps, with the stylus approach described below	[Kiesewetter]
Measure the **electrostatic pull-in** voltages of structures made from the film under test	The pull-in voltage is sharply defined, so high precision is possible; the test suite also provides information on Poisson's ratio and residual stress	Processing of structures is complex; high accuracy relies on measurement of manufacturing imperfections; insulating films must be sputtered with metal first	[Osterberg] ('M-Test')
Deform the material under test in an external **tensile testing machine**	Can call on existing test standards	Laborious; apparatus not available in a majority of MEMS labs	[Sharpe]
Check for variations in the **resistivity** of a film	Ideal for a mature process where variation must simply be minimised	Does not give an absolute value for *E*; not possible on insulators	[Analog]
Scan a **stylus profilometer** along a test cantilever or bridge and measure deflection	Can compensate for processing imperfections with appropriate data analysis	Variation of the force applied by the profilometer is yet to be calibrated; reliable processing of data difficult	[Denhoff], [Tai]

Of these methods, the M-Test exhibits the best accuracy — about 3.5% uncertainty in the *E* of bonded silicon-on-insulator — but its complexity has precluded adoption in the 7 years since its publication. We wish to design a test method that gives less than 10% uncertainty in *E* with much less processing and measurement effort than the M-Test requires. We are setting aside the desire also to know Poisson's ratio and residual stress. In this

Department, [Hopcroft] *et al.* have pursued the use of a surface profilometer to deflect cantilevers, but a robust way of extracting the modulus from data exhibiting dust and beam vibration has yet to be demonstrated. The remainder of this section describes work aiming to provide such an extraction technique.

Figure 12: Beam plan and section

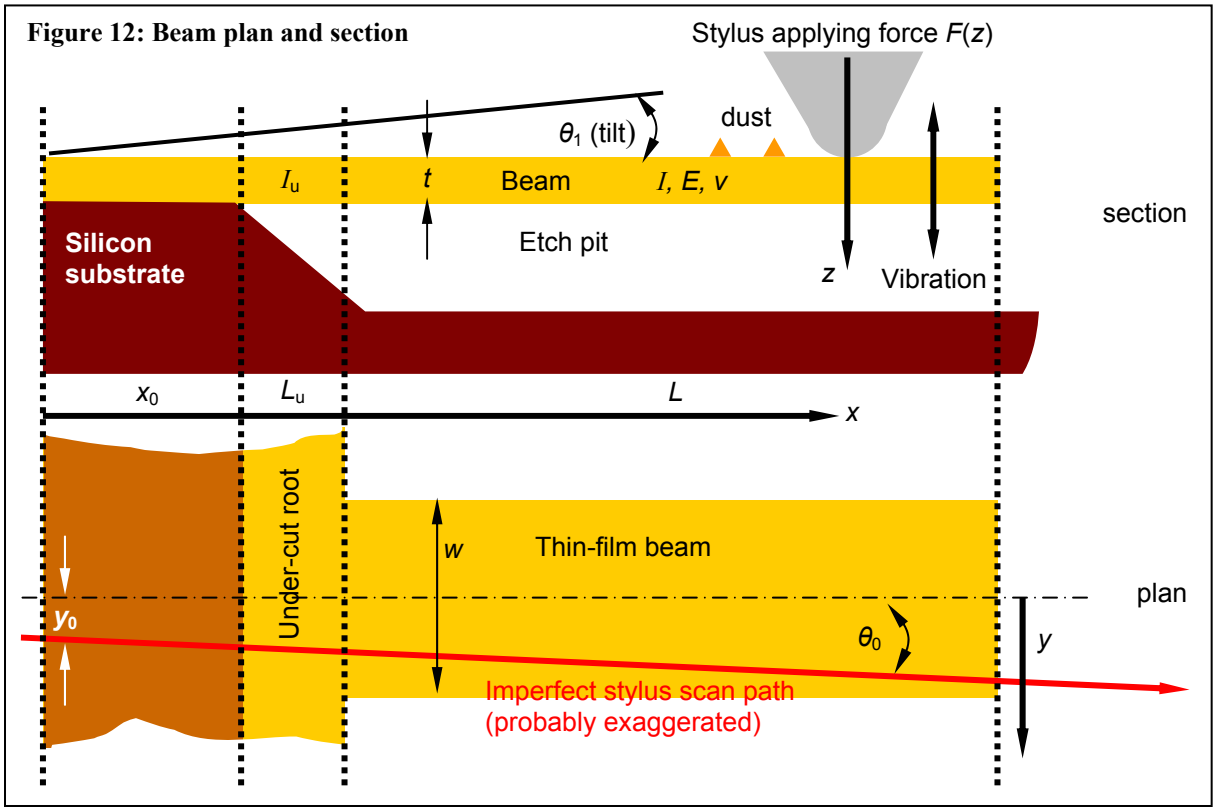

Beam-bending theory and stylus scanning model

Figure 12 above shows a section and plan of an imperfect cantilever beam being scanned by an imperfect stylus profilometer. The cantilever is made by patterning the thin film and under-etching the substrate. The profilometer then scans from root to tip, applying a nominally constant force selected by the operator. The beam deflects and yields a position–displacement (x–z) trace. If deflections in z can be considered small, if the stylus scans perfectly centrally and if we model the under-cut root as a short, different-width beam of the same material, the deflection can be written, where $N(x)$ is noise on the trace, as:

$$z(x) = \left(\frac{F}{E}\right)\left\{\frac{L_u^{\,3}}{3I_u} + \frac{L_u^{\,2}\left(x - x_0 - L_u\right)}{I_u} + \frac{L_u\left(x - x_0 - L_u\right)^2}{I_u} + \frac{x^3}{3I}\right\} + N(x) = \left(\frac{F}{3EI}\right)x^3 + O(x^2) + N(x) \quad \ldots 1$$

O(x^2) means terms in x^2, x and x^0. It is clear that the term in x^3 is independent both of the starting position of the stylus and of the extent of any under-cutting at the root. It is this property of the method that makes it potentially accurate, yet easy to execute: we would like to probe this cubic coefficient in isolation. Real data are not, however, this simple and the likely effects on $z(x)$ of each possible imperfection are summarised in Table 4 below.

Table 4: Beam bending variables and their effects. Yellow: error inevitably impacts E's estimate; Blue: impact on E's estimate depends on design of test structure; Green: impact on E's estimate depends on extraction algorithm. Formulae are taken from [Mencík].

Variable or factor	Description	Expression for impact on vertical deflection	How error affects $z(x)$	Likely % error introduced for the chosen test structure (see next sec.)
z	Vertical deflection of stylus tip (+ve down)			
x	Position of stylus on beam			
L	Length of beam			
E	Young's modulus			
w	Width of beam		Linearly	(10/290) = 3.4%
t	Thickness of beam		Cubically	3 × (0.03/2.39) = 3.8%
I	= $wt^3/12$		See w and t	5.1%
ν	Poisson's ratio	Neglecting plate modulus effects overestimates E by a factor of as much as $(1 - \nu^2)$		From simulation, max. 2.5%
L_u	Length of under-cut		Affects terms in x^2, x and x^0	
I_u	Second moment of area of under-cut		Affects terms in x^2, x and x^0	
Self-weight of cantilever	$\frac{3\rho L^4}{2Et^2}$ where ρ = density		~ x^4	$\frac{3\rho wtL}{8F}$ = 0.004% at tip (ρ = 3440 kgm^{-3}) Below noise of profilometer.
θ_0	Stylus angular offset from centre-line of beam		x-axis in profilometer trace scaled by cos θ_0	Term in x^3 underestimated by factor cos^3 0.29 = 0.88.
y_0	Stylus linear offset from centre-line of beam			
Torsion of cantilever	$\frac{Fx(1+\nu)}{2EI\gamma}(\theta_0 x + y_0)^2$ where γ is a factor depending on w and t that is taken to be 1 when w much larger than t		For $y_0 > 0$ torsional deflection the impact goes as x; for $\theta_0 > 0$ it goes as x^3.	Max 18% in actual deflection if stylus leaves beam at corner of tip, but counteracted by stretched x-axis in the case of angular misalignmnents.
Local deformation and indentation	Hertzian contact: $\left(\frac{9F^2}{16RE^{*2}}\right)^{1/3}$ where R = tip radius and $E^* = E/[2(1-\nu^2)]$ assuming stylus and beam to have same E. Local deflection: $\frac{6F\left(1-\frac{2}{\pi}\right)(1-\nu^2)w^2}{Et^3\pi^3}$		Const.	Hertzian (assuming 8μm tip radius): 10^{-11}m so below noise of profilometer and constant anyway; negligible. Local deflection: ~20nm, about 3% of deflection when stylus is at tip of beam; since it is constant (except very near the root) it should be eradicable.
Shear deformation	$\frac{12Fx(1+\nu)}{5Ewt}$		x	86pm at tip: negligible
x_0	Distance of stylus starting point from root of beam		Affects terms in x^2, x and x^0	
κ_0	Initial curvature of beam (owing to residual stress gradient in released beam)		If κ_0 is constant along the beam it contributes to the term in x^2	
θ_1	Tilt of sample out of horizontal		Adds to the term in x	
F_0	Nominal stylus force		Linearly	
k_F	Spring constant of stylus mechanism		Linearly, but effect varies with z	
r_{tip}	Stylus tip radius	Complex effect for large deflections: stylus exerts non-vertical force.		
Large z deflections	Cause E to be underestimated if the assumption of small, linear deflections is used erroneously			
Noise on trace	A complicated signal results from dust on the beam and from vibration of the beam and possibly of the stylus mechanism. Noise may have components in x^3 but is extremely difficult to model.			

Errors in the beam width and thickness and in the stylus force inevitably affect the extracted modulus and must be controlled individually. Of the remaining errors, potentially the most problematic are those arising from beam torsion, anticlastic effects, non-linear deflections, and noise on the trace. To exploit the elegance that profilometer scanning promises, we need firstly to minimise the impact of these effects on the deflection term in x^3, and secondly to stop the $O(x^2)$ terms biasing the modulus that we extract. The first aim can be achieved by careful design of the test, and the second by devising a robust algorithm to analyse the data.

Designing a test

We wish to minimise the total processing and measurement time, and to allow the whole procedure to be performed by technicians in any MEMS laboratory, without special training. Apparatus would ideally be restricted to a stylus profilometer, an optical microscope, and that needed to measure the film's thickness, pattern it, and etch away the substrate.

Figure 13: Candidate test beam shapes; impact of large deflections on point of force application

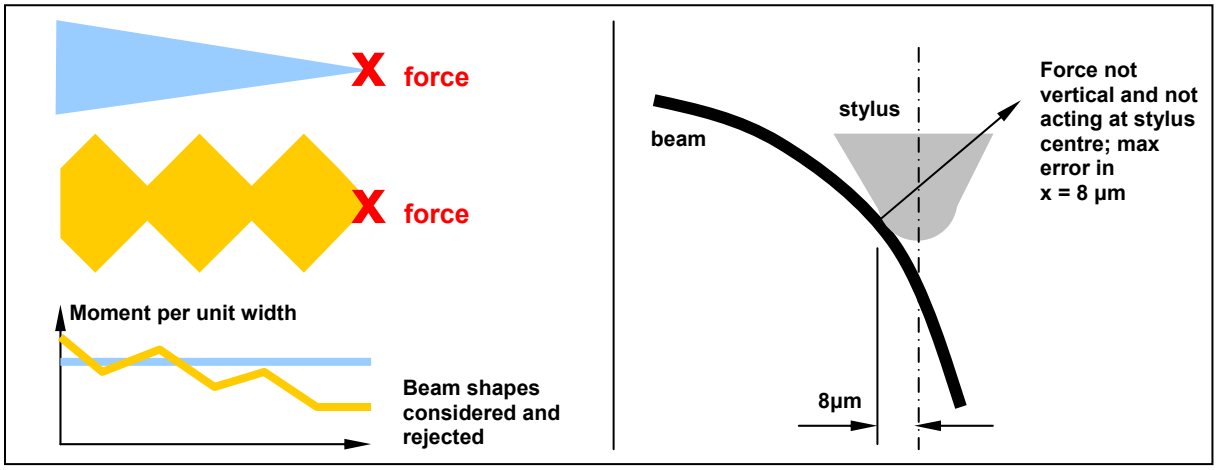

The best **shape** for the beam was the subject of early investigation. While a triangular beam loaded at its sharp tip experiences constant moment per unit width, and might therefore be useful for determining the yield stress of a film, it would be extremely difficult to align the profilometer path with the central axis and the design offers no obvious advantage for determining the elastic modulus. Beams with a 'zig-zag' profile were also designed and made in an attempt to see whether, by introducing periodicity to the trace, extraction of the modulus became any more reliable. Yield was poor and stylus alignment difficult, and the idea was abandoned. So there is no proven merit in using a test beam that is anything other than rectangular. For a film of given nominal E and t, the problem is thus reduced to choosing the width and length of a test beam and the force used to deflect it. Each choice is difficult.

The **forces** available range from approximately 0.3μN to 1000μN but depend on the particular machine. If the absolute uncertainty of the force is independent of the selected nominal force, the use of large forces would make the proportional uncertainty of force smaller. A test method requiring larger forces would be accessible to more laboratories: the smallest forces are available only from newer machines. Using larger bending deflections might even allow initial curvature in the beam (arising from relieved stress gradients) to be ignored. On the other hand, smaller forces would allow deflections to be kept in the linear regime, making analysis easier: if $z/x < 0.1$, the deviation from the Euler approximation used in Equation 1 is less than 1% [Riley] and the effects of anticlastic curvature are also restricted. For small deflections, the radius of the stylus (typically 8μm) is unimportant; for large deflections the force would no longer be applied vertically (Figure 13). Moreover, using small forces allows us to avoid fixing the sample to the machine without the risk of its slipping during scanning. Not fixing the sample avoids damage to the stylus. On balance, it seems intuitively sensible to gather simple data instead of processing complicated large-deflection traces; so smaller forces will be employed here.

The **width** of the beam needs to be large enough that the stylus is unlikely to fall off the side of the cantilever during scanning: in practice a width of 300μm has proved usable with ease. A wider beam allows a larger force to be employed with less z deflection, thus combining two of the benefits described above. Beams that are too wide, however, will tend to behave like plates with larger apparent moduli, which would need to be allowed for in the analysis. The beam **length**, meanwhile, needs to be small enough that it does not hit the bottom of the etch pit in the substrate during deflection, and yet long enough to obtain enough data points.

There are two other considerations. Firstly we may wish to have more than one beam per test site. With newer profilometers, including the Veeco [Dektak] 8 available in this Department, it is possible to pre-programme a series of traces at different positions on the sample; so many traces can be obtained with minimal extra effort. The spread of the resulting set of extracted moduli would provide a valuable insight into the consistency of the procedure, and would allow particularly bad traces to be identified and discarded. Secondly, the smaller we can keep the under-cutting at the root, the smaller the $O(x^2)$ terms will be and the easier the data should be to analyse. When the substrate etch is anisotropic (e.g. KOH etching of Si), the alignment of the test design and the substrate is important (Figure 14). A design that minimises the sensitivity of under-cut to misalignment with the substrate crystal axes would be a boon.

Figure 14: The importance of aligning the mask design with the crystal axes.

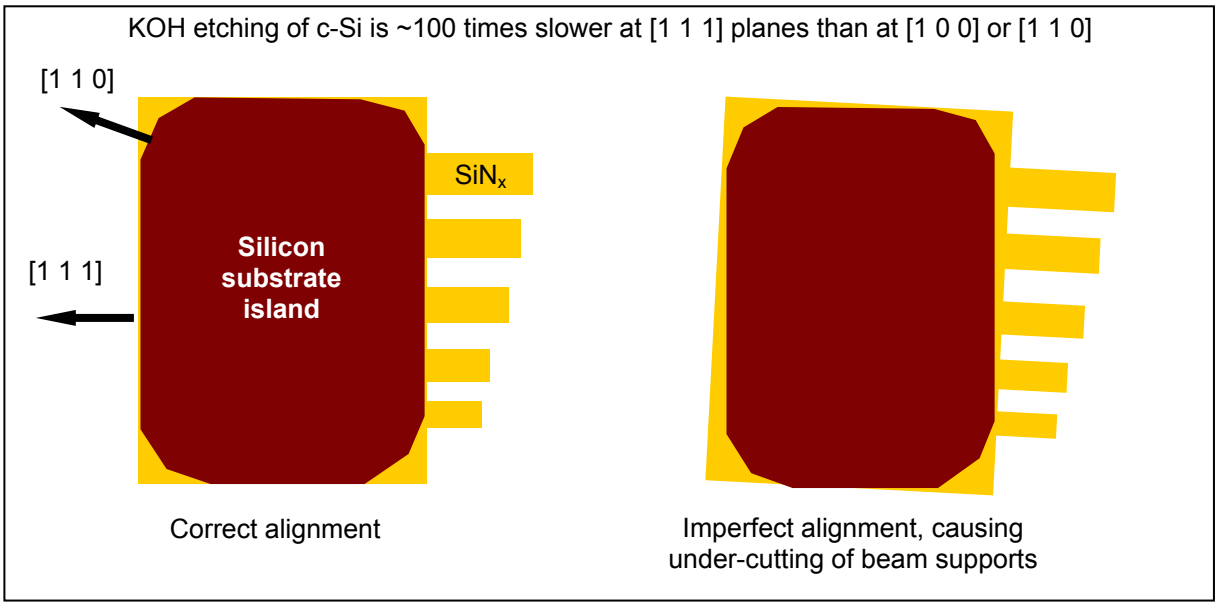

The site designed is shown in Figure 15. All 20 beams face the same way, so that they can all be scanned without removing the sample from the machine (the stylus scans in one direction only). The beams are 500µm long and 300µm wide, and can be patterned either by laser ablation or by photolithography and reactive ion etching. We would like $z/x < 0.1$ everywhere, so applying the condition at the tip that

$$\frac{z}{L} = \frac{4FL^2}{Ewt^3} < 0.1$$

and substituting a 16.7µN force, we require that $Et^3 > 5.6 \cdot 10^{-7}$ Nm. A film on which this method has been tested is silicon nitride with E = 170GPa and t = 2.39µm approximately, giving $Et^3 = 2.3 \cdot 10^{-6}$ Nm, safely above the limit. It is clear that the usability of a particular test structure will be governed by a minimum (Et^3/F): one design will therefore be usable on many different films, and its versatility will increase rapidly with thickness. One drawback of placing all the beams in a single trench is that a slight rotation of the design relative to the silicon substrate can lead to a large under-cut when the silicon substrate is etched in KOH. In practice, it has proved possible to achieve under-cuts of less than 10µm by careful laser micromachining.

We also need to be aware of how the test site will perform if **misaligned in the profilometer**. If the stylus loads the beam off-centre at any time, the beam will deflect more than it would if loaded centrally. As Table 4 showed, deflections due to torsion will contribute a term in x^3 to the deflection if the stylus starts at the centre of the root but travels along the beam at an angle θ_0 to the longitudinal axis. If, however, the stylus travels parallel to the axis but offset by y_0, the extra deflection increases as x. The susceptibility of the test site to errors

from torsion is considered in Figure 16(a), where the percentage increase in z resulting from added torsion is plotted against *true* stylus position, x. The green lines are not in fact valid near the root, where the beam is obviously clamped and cannot twist as much as the model predicts. Large extra deflections in x^3 are troubling because E cannot then be extracted without making an estimate of the torsion, and hence of Poisson's ratio. The magnitude of the change in the x^3 term increases quadratically with angular offset, so although the largest increase in deflection possible for this test site is 18% (if the stylus leaves the beam at its corner), more realistic misalignments would yield much smaller increases. Moreover, because angular misorientation of the stylus 'stretches' the x-axis of the profilometer trace, the error's size will be reduced. For a misalignment of θ_0, the recorded x values, x_{rec}, will be related to the true x values x_{true} by $x_{true} = x_{rec}\cos\theta_0$. For a perfect scan, $z = Fx_{rec}^3/3EI$; for one at angle θ_0, $z = [F/3EI + F(1+\nu)\theta_0^2/2EI]x_{rec}^3\cos^3\theta_0$. The ratio of these deflections simplifies to $(1 + 1.5\nu\theta_0^2)$ if we expand up to terms in θ_0^2. For the designed test site and the largest possible θ_0 the error in the extracted modulus due to angular stylus misalignment will not actually exceed 4%. *Parallel* misalignments y_0 (where x is *not* stretched) are therefore of greater concern.

Figure 15: Test site design

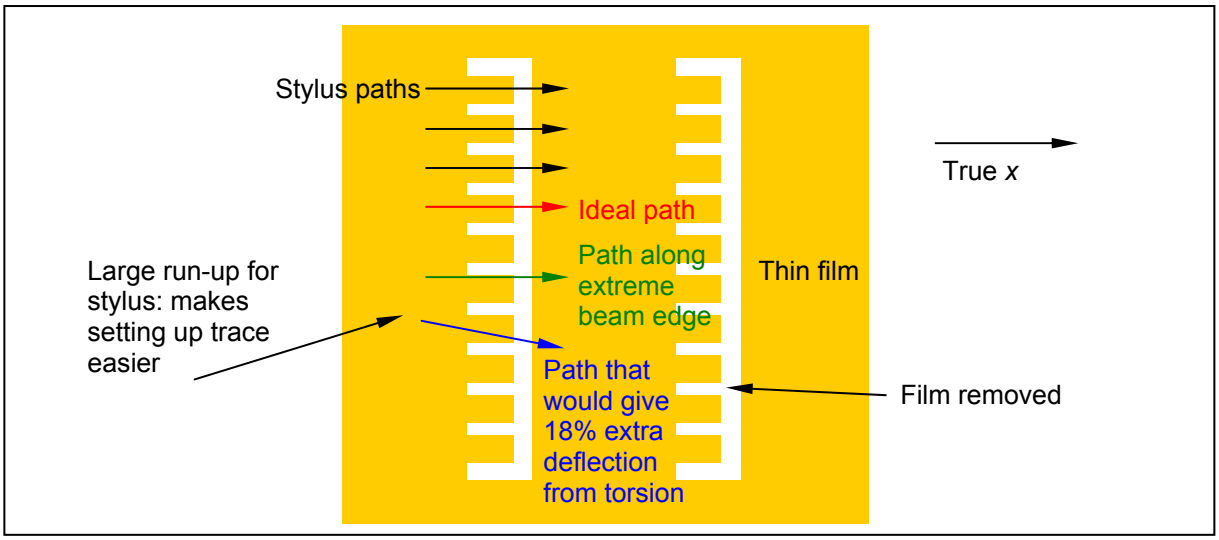

An attempt to predict the impact of **anticlastic curvature**, and of any **departure from the linear deflection regime**, is shown in Figure 16(b), where Matlab-simulated results are normalised against the deflections predicted by a simple cubic model for a beam with no under-cut at its root. The simulation exploits the derivation given by [Ashwell] that states the effective elastic modulus, E_{eff}, in terms of ν and the non-dimensional $(w^2\kappa/t)$, where κ is the beam's longitudinal curvature. E_{eff} tends to $E/(1 - \nu^2)$ for large $(w^2\kappa/t)$. The reason the effective modulus increases with $(w^2\kappa/t)$ is that the beam's anticlastic curvature increases with $(w^2\kappa/t)$, increasing the effective second moment of area of the beam or plate and hence its

stiffness. The following procedure was executed numerically for each stylus position λ between 0 and L in turn:

1. Initially assume $dz/dx = 0$ and $E_{\text{eff}} = E$ for all x between 0 and λ.
2. Define bending moment $M(x) = F(\lambda - x)$.
3. Evaluate $\dfrac{d^2z}{dx^2} = M\left[1+\left(\dfrac{dz}{dx}\right)^2\right]^{3/2} \Big/ E_{eff}(x)I$ for all x between 0 and λ. [Riley]
4. Evaluate $\dfrac{dz}{dx} = \int \dfrac{d^2z}{dx^2}\,dx$ for all x between 0 and λ.
5. Evaluate $z = \int \dfrac{dz}{dx}\,dx$ for all x between 0 and λ.
6. Use [Ashwell] to evaluate $E_{\text{eff}}(x)$ for all x between 0 and λ.
7. Repeat steps 3–6 until z converges.
8. Take $z(\lambda)$ as the deflection for the final profilometer trace at $x = \lambda$.

Figure 16: (a) torsion effects; (b) onset of 'large' deflections and anticlastic effects in test site

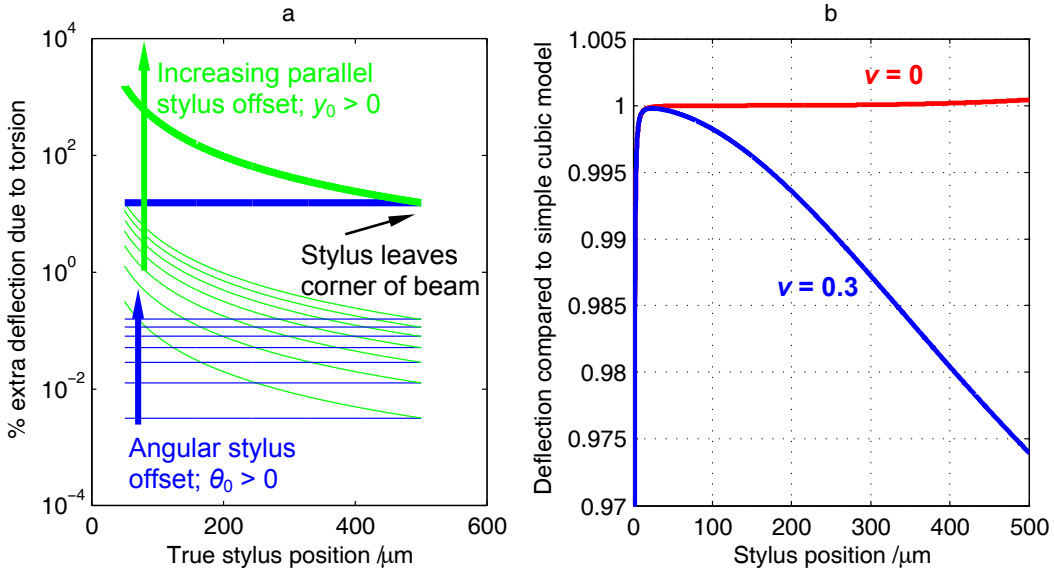

Results did not refine appreciably for a dx smaller than 0.25μm, and results always converged after 4 iterations. Setting $\nu = 0$, the effect of non-linear deformations was considered in isolation and an error of less than 0.1% was confirmed for this particular test site. For $\nu = 0.3$ the method still overestimates deflections because, significantly, it neglects the fact that the beam is clamped at the root, so that for very small x the effective modulus is pinned to the plate modulus, exactly $E/(1 - \nu^2)$. This simulation is useful, however, because it shows that the x–z trace is no longer a simple polynomial, and therefore that the impact of anticlastic curvature on the performance of any fitting algorithm may be unpredictable.

Extracting the modulus from real data

A typical profilometer trace is shown in Figure 17. Three imperfections are immediately obvious. Firstly the sample is tilted, adding a significant term in x to the trace. Secondly, there are large spikes on the trace, attributable to dirt on the surface of the beam (the adjacent photograph of the sample confirms this). Thirdly, the beam started to vibrate as the stylus reached its tip. More careful processing has been shown to yield cleaner samples and better traces but sometimes a very clean environment is not possible and we also want to see whether we can afford to do processing quickly and with minimal care. Moreover, we may wish to test rough films such as electroplated Ni and in that case a jagged trace is inevitable.

Figure 17: Typical Dektak trace; optical micrograph of several beams on the prototype test site

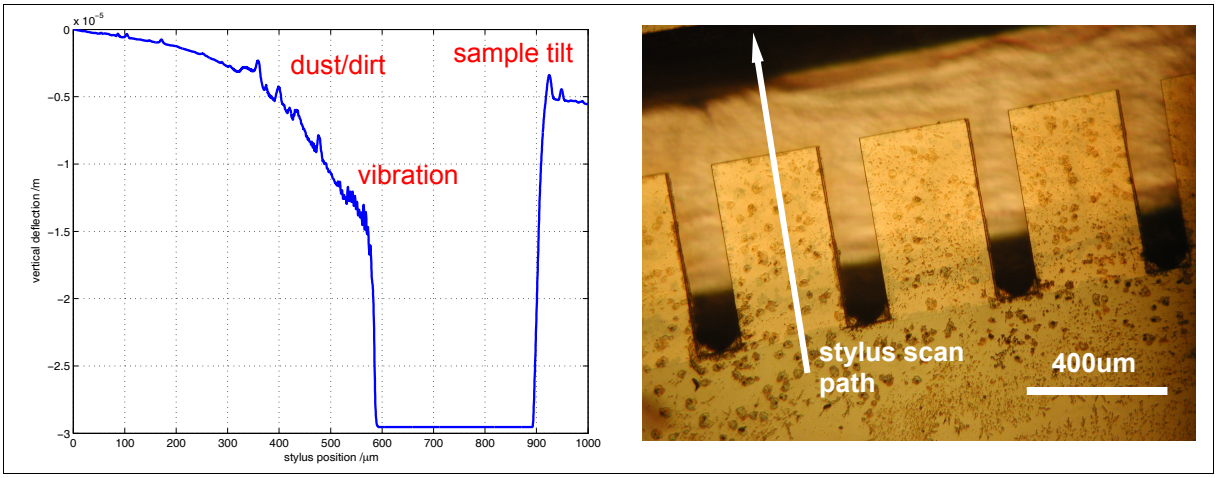

The challenge in processing a trace such as this is best summarised by considering the most basic way of trying to extract E. Because we want to identify the term in x^3 in Equation 1, we might imagine that performing a straightforward least-squares fit of a cubic polynomial to the data would yield the answer. Figure 18 shows the main reason why not: the best-fit cubic coefficient is extremely sensitive to noise in the trace. If a dust spike happens to fall at an edge of the range of data that is used, the cubic coefficient may even change sign. It cannot be guaranteed that an operator would avoid choosing such a range. Even when the noise is not as gross as this, it is normal for a large range of combinations of polynomial coefficients to offer equally close fits to the noisy data. In other words, there is strong collinearity between the deflection terms in x^3, x^2 and x.

Pre-processing the data. Intuitively, collinearity should become less of a problem if the magnitudes of the x^2 and x terms can be made smaller relative to those in x^3. This may be partly achieved by eliminating sample tilt and any initial beam curvature: we can calculate the differences in deflections between two traces performed consecutively under different loads, and assume the resulting 'virtual' trace to have been taken under the difference of the two

loads. If initial curvature is known to be negligible, we can eliminate tilt more simply by ensuring that the stylus rides up on to the opposite bank of the etch pit and defining a line joining the cantilever root and the opposite bank to be horizontal.

Figure 18: Impact of dust-like noise on modulus extraction

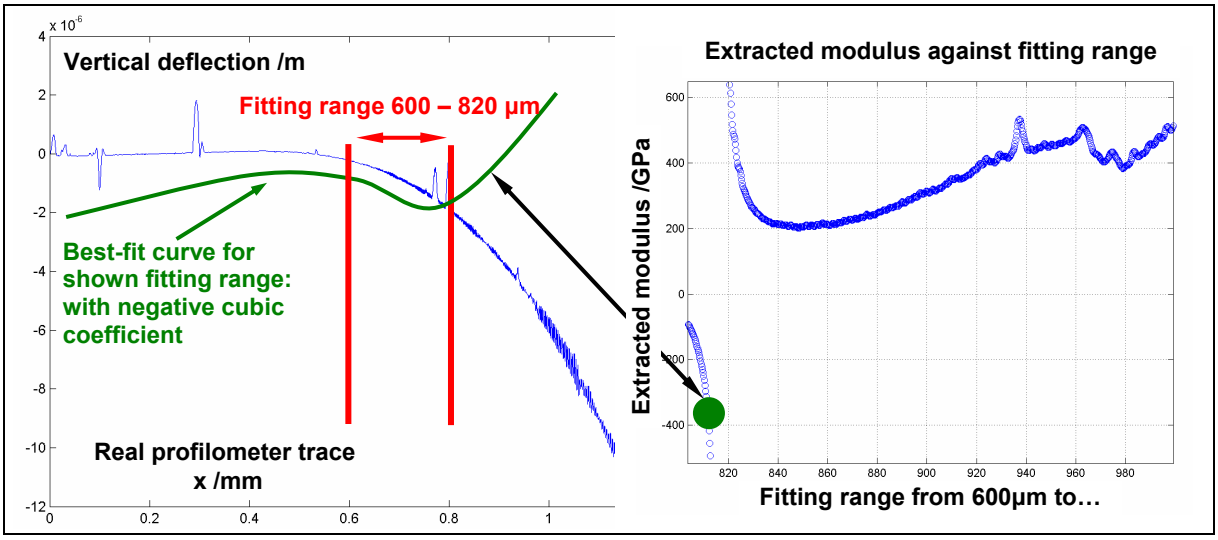

Removing noise from the trace is a much harder task. Although it may at first seem that taking the difference between two consecutive traces should also eliminate the spikes caused by dust, in practice either the sample slips slightly in *x* between traces or the stylus path changes: noise remains.

One possibility considered was to apply a median filter to the data, but this proved not to work because the overall slope of a trace is generally so great that dust does not cause the trace to spike out of the range occupied by the rest of the data in the median window: hence the spikes are only slightly smoothed.

Manual rejection of dust spikes by the operator has been tried by [Hopcroft]: a graphical user interface prompts the user to select regions of data that are to be rejected. This may be a good solution when there are a few obvious small spikes, but for data such as that shown in Figure 17 it would be impossible for a human to decide by inspection what to reject and what to keep.

Choosing an extraction algorithm. It therefore seems that what is needed is an algorithm that can extract the modulus reliably from data without requiring the noise to be removed first. An important consideration here is that the noise tends to be asymmetric: dust is always on *top* of the beam. Simply smoothing the data or rejecting outliers *after* some initial fit will therefore leave bias in the result, and the modulus will tend to be overestimated. With this challenge in mind five strategies were evaluated to extract the modulus from the data:

1. **Range variation, polynomial**. After prompting the user to select as large a range of valid data from the trace as possible, a series of third-order polynomial fits is made to the data, using a differently sized range of data each time. One end of the range is fixed and its size is varied from 100μm up to the maximum specified range. The third-order coefficient of each best-fit polynomial is taken to equal ($F/3EI$). The standard deviation of the distribution of moduli extracted during the process is taken as the uncertainty of the extraction. This is the basic method illustrated in Figure 18.

2. $z^{1/3}$ is plotted against x and a straight line is fitted to the data over a number of ranges. Its gradient is taken to equal $(F/3EI)^{1/3}$. Terms in x^2, x and x^0 now inevitably introduce bias to the extracted value but if they can be kept small this method may provide the best answers because, with only one fitting variable, the problem of collinearity is removed. The ranges are selected in one of two ways:
    a. **Range variation, cube root.** As in strategy 1, we specify extreme limits for the fitting range, and the range is automatically varied within those limits and a fit performed each time. The uncertainty is taken as the standard deviation of the distribution of extracted E.
    b. **Manual straight-line fitting**. A graph of $z^{1/3}$ against x is plotted and the operator prompted to click on the end points of what they perceive to be two plausible best fit lines. The uncertainty is taken as half the difference between the two extracted E values.

3. **Successive Rejection**. The user selects a range of valid data, and a sequence of third-order polynomial fits is made to the data. After each fit the 1% of remaining data points that lie furthest from the fitted curve are discarded, and the next fit is performed on the reduced data set. After, say, 200 cycles the extracted modulus should have stabilised and its value can be taken. The standard deviation of all the intermediate extracted values could be taken as a notional value for the uncertainty.

4. **Resampling**. The user selects a range of data, and a series of random sub-samples is made from that data, in each of which, say, 10% of the data are chosen. A third-order polynomial fit is performed to each sub-sample and a distribution of extracted moduli is built up. If a small enough proportion of data is sampled each time, some of the extracted moduli will be completely free from bias caused by the dust. We might expect a bi-modal distribution in which the mode at the lower modulus corresponds to the correct value.

Figure 19: illustration of candidate data analysis methods 2(a), 3 and 4.

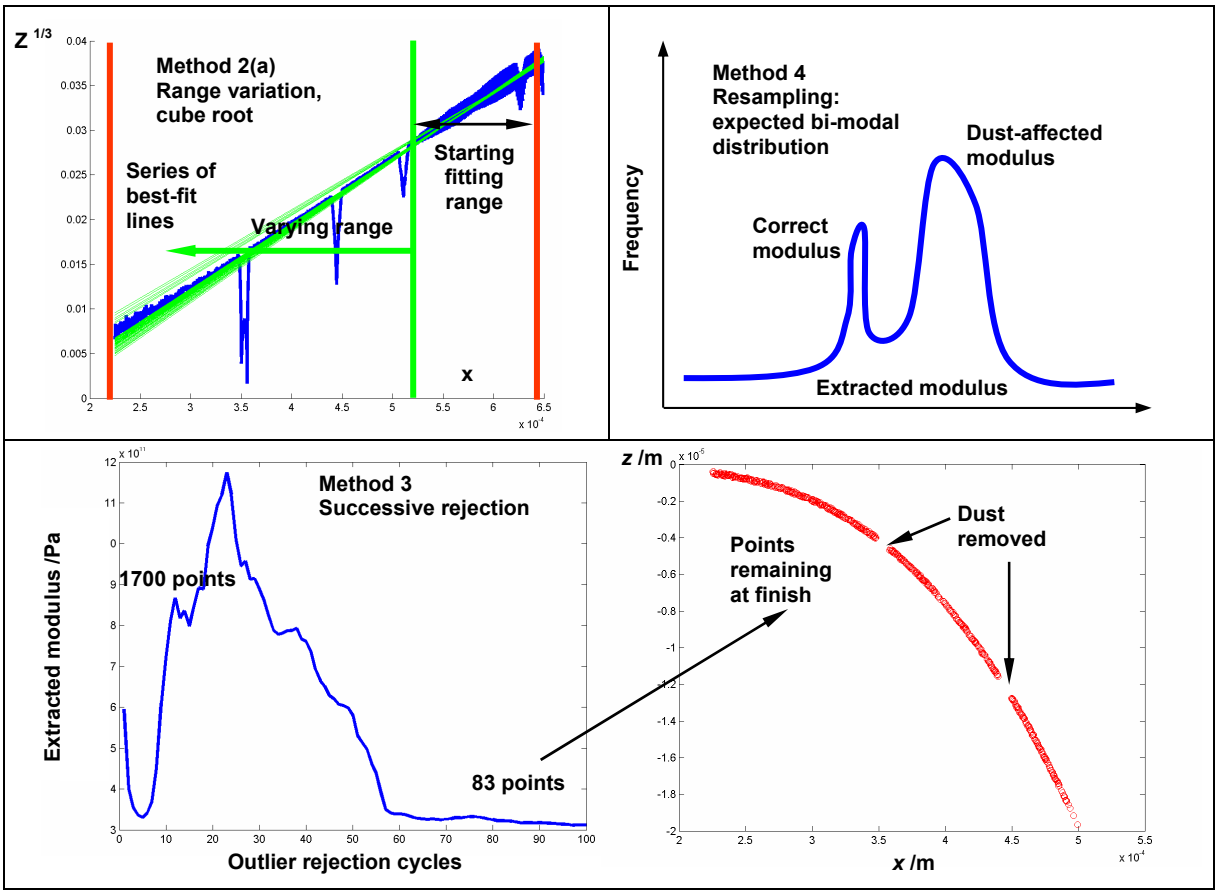

Figure 20: Eextract user interface

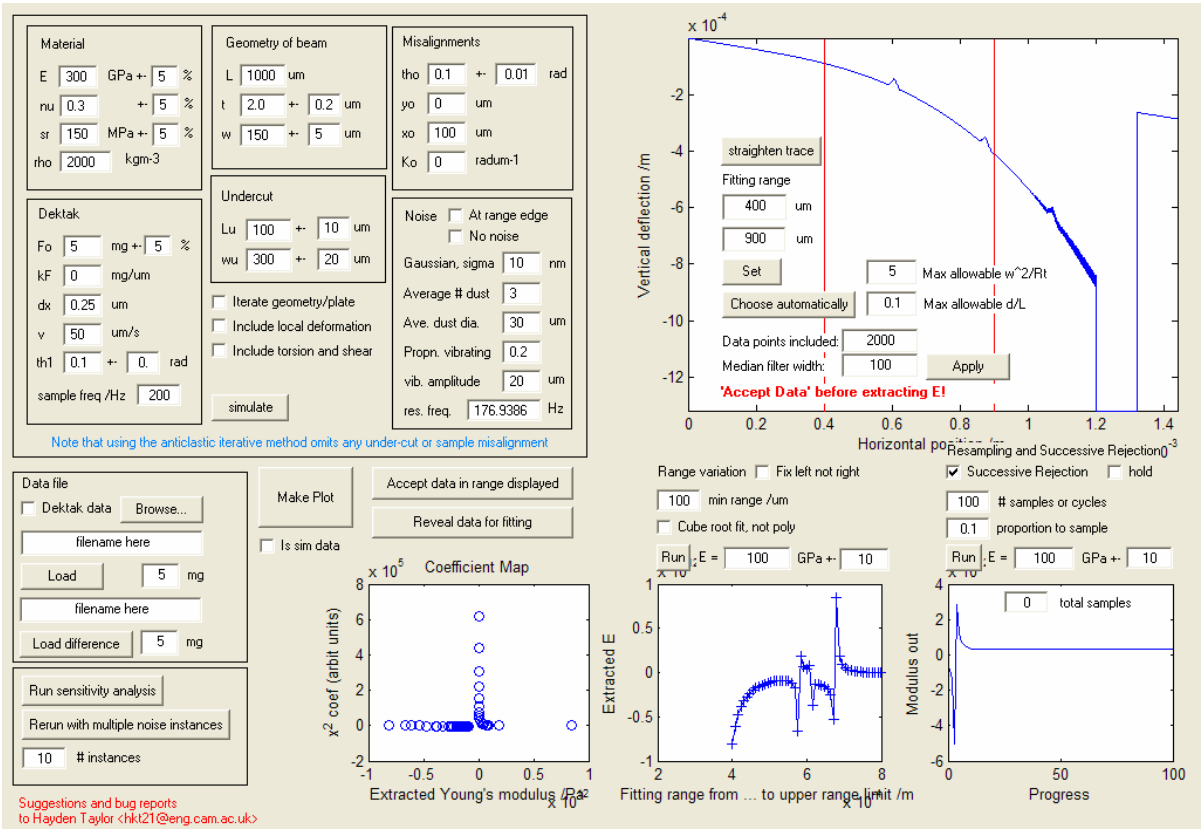

Figure 19 illustrates strategies 2 to 4. All five methods were programmed in Matlab and a graphical user interface, *Eextract*, was produced to allow easy comparison of the methods. *Eextract* is illustrated in Figure 20. The interface can import real profilometer data or simulate a trace in which root under-cutting, misalignments and superimposed noise can all be varied by the user. Simulated traces are useful for testing fitting algorithms because the true modulus is known and the closeness of the fitted solution to that true modulus can be used as a measure of the quality of the algorithm. The performance of these methods using real and simulated data will now be compared.

Results and discussion

Let us first assess the performance of each of the candidate fitting procedures on three types of profilometer trace, one real and two simulated; the results are reported in Table 5 below:

1. A real trace taken from the test site described above. It was rather 'cleaner' than that shown in Figure 17 but still exhibited distinct imperfections (**A**);
2. Iterative non-linear simulations including anticlastic effects but no noise (**B**, **C**);
3. Simulated traces using a pure polynomial and superimposing a crude noise model (**D**, **E**).

Table 5: Performance of candidate extraction procedures

Values in GPa	Real data: trace 3 from test site (**A**)		Noise-free simulation with non-linear deflections. ('True' E = 178.5GPa.)				Ideal third-order polynomial simulation with superimposed noise, including triangular 'dust', sinusoidal vibration and Gaussian noise. ('True' *E* = 178.5GPa.)			
			v = 0.3 (**B**)		*v* = 0 'sanity check' (**C**)		Gaussian noise with σ = 85nm (**D**)		Gaussian noise with σ = 1.7μm (**E**)	
	μ	σ	μ	σ	μ	σ	μ	σ	μ	σ
1: Range variation: polynomial	181.9	614.8	186.0	2.6	178.5	0.0	180.9	148.2	170.9	446.6
2(a): Range variation: cube root	273.5	30.0	181.4	1.2	178.5	0.0	178.3	1.2	177.1	1.0
2(b): Manual cube root	219.1	14.0	187.5	3.4	178.7	0.3	177.0	2.3	168.3	10.2
3: Successive rejection	180.2	3.9	194.8	1.2	178.5	0.0	264.0	30.6	212.0	14.6
4: Resampling	188.7	11.1	190.1	0.2	178.3	0.0	176.8	34.2	172.0	72.6

Considering the real data to begin with, methods 1, 3, and 4 give results that are consistent with one another, but methods 2(a) and 2(b), relying on a straight-line fit to the cube root of the data, are inconsistent with the others. Although under-cut appeared, from an optical micrograph of the test site, to be negligible, it is possible that there was some invisible defect at the root of the test site (e.g. a compressible support) that increased the term in x^2 and led to such a bias. We gain further support for this inference when we consider that, in the

case of the simulated data with superimposed noise but *no* under-cut (**D**, **E**), a discrepancy between method 2 and the others is *not* present: in fact method 3 gives a much larger result. The bigger the under-cut the less attractive the straight-line fitting methods, 2, will probably become. [He] *et al.* are doing extensive work on this question in this Department.

The amplitude of the superimposed Gaussian noise strongly affects the result of method 3 and the variance of method 4's result: since such a small change in the noise can cause such a large difference in results, it may well be that the noise model employed is completely wrong. The bi-modal distributions hoped for with method 4 did not emerge.

When we apply the candidate extraction methods to the noise-free simulation including anticlastic effects, **B**, the procedures that attempt to fit a polynomial to the data readily make errors. Although the largest difference between the simulated deflection in **B** and a simple cubic model was 2.5% (see Figure 16), the final error in E extracted from trace **B** is inflated to as much as 9%. It becomes clear that with the present test site, errors encountered in processing the data will be systematic as well as simply due to noise.

The standard deviations in Table 5 above do not include uncertainties in beam dimensions or applied forces; they arise purely from the behaviour of each algorithm. We can see immediately that the traces including noise lead to large variances in the moduli extracted by method 1: it is not a robust procedure. The standard deviation yielded by method 4, however, is much smaller (corresponding to a 6% uncertainty) when the method acts on the real data (**A**) than when it acts on the *simulated* noisy data (**D**, **E**). Again, it is entirely possible that the noise model used in the simulation was unrealistic.

There is no one clear way forward based on what has been observed. For the real data, the smallest variances in E are encountered for methods 3 and 4, with method 3, successive rejection, having the smallest standard deviation by a factor of 3. That method 3 also suffers the greatest bias when operating on trace **B** (simulated anticlastic curvature), however, makes it less attractive: its impression of accuracy may well be erroneous.

We now move on to consider **trace-to-trace consistency**. The five candidate procedures were applied to each of 20 traces from nominally identical beams on the test site and the results compared. The results for three of the methods are shown in Figure 21 below.

It emerges that method 2(b) — involving manual selection of a best-fit line — tends to yield more consistent results than allowing the programme to perform the fitting itself (method 2(a)). This is because certain traces may appear, when viewed in x–z form, to have a particular region of 'good' data which, when cube-rooted, actually turns out to be rather jagged for smaller deflections. Hence it seems better for the user to intervene when shown the

x–$z^{1/3}$ graph. Method 1 was discarded as being too unstable. Trace 4 exhibits unusually large uncertainty in its extracted moduli: it is the trace illustrated in Figure 17 and is evidently an atypically noisy one.

Figure 21: Consistency of extracted Young's moduli for SiN[TM] patterned with a test site of 20 beams

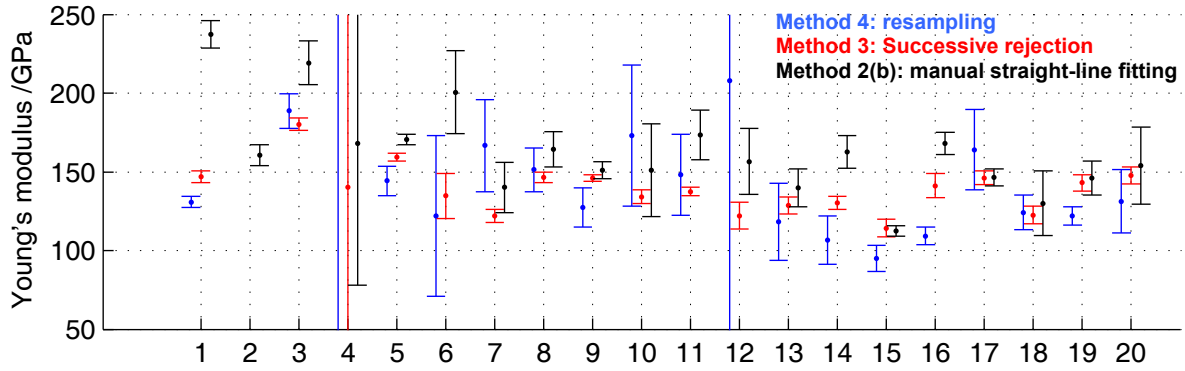

As the user progressed from trace 1 to 20 they appeared to get better at aligning the stylus with the beams: the consistency generally improves. This trend demonstrates that manual skill, during both data acquisition and analysis, remains a significant factor in the quality of the test. The extracted mean moduli for traces 5–20 have the following statistics:

Table 6: Statistics of moduli extracted from test site

Values in GPa	Mean extracted *E*	Standard deviation of extracted mean *E* values.	'Overall' standard deviation including individual uncertainties
2b: Manual straight line fitting	154.1	20.1	34.0
3: Successive rejection	137.4	12.2	17.5
4: Resampling	138.2	29.2	92.8

A crude way of estimating the total uncertainty in the extracted modulus is to add the standard deviation of the extracted mean moduli (the third column above) to the average standard deviation of the individual extractions (all the separate error bars in Figure 21). It emerges that the three methods give results consistent with one another but that uncertainties are large. Method 3 offers the least uncertainty, but the estimate above indicates that a 13% error exists even without accounting for dimensional and force errors.

Reasons for the variation in extracted modulus from trace to trace probably stem from differences in the noise. Dirt was distributed unevenly across the sample and some traces were consequently much less smooth than others. Another clear possibility is that torsion was introducing variable errors: the parallel offset of the stylus from the beam centre would have been different for each trace and *could* have contributed an error in excess of 10% according to the analysis above. Since stylus orientations were not recorded, this cannot be confirmed.

If we include estimated errors of 10% in the force, 2.1% in the thickness (from [He1]) and 3.4% in the width (measured from an optical micrograph), the uncertainty obtained using

method 4 becomes 17%. Since much of this comes from the extraction method, there certainly seems to be scope to improve the accuracy by refining the test site design, cleaning the sample before testing, and employing greater skill during the scanning.

All the moduli extracted are far lower than literature values for ideal stoichiometric silicon nitride, which are in the region of 300GPa. The silicon-rich composition of the LPCVD SiN_x discussed here could explain the lower modulus: with interstitial Si atoms pushing atoms in the Si_3N_4 structure apart, the material's atomic structure will probably be less dense, and hence less stiff, than for stoichiometric material.

For comparison, an attempt was made to check the modulus of the film by the resonance method (Table 3). The sample of 20 beams was glued to a piezoelectric buzzer which was then actuated at frequencies swept from 10Hz to 100kHz using a signal generator. The beam was viewed under an optical microscope and a blurred image of the beam was expected at resonance. We would expect the fundamental resonance frequency of the beams on the test site to be $(1/2\pi)(EI/\rho A)^{0.5}(1.875/L)^2$ [Conradie] where A is the beam's surface area. This evaluates to about 800Hz. No blurring was seen at any frequency. It is probable that the beams tested were too short, and stiff, to amplify sufficiently the few microns by which the substrate was being moved. The sample was then placed under a Zygo interferometer and it was expected that the greatest blurring of interference fringes would be observed at resonance. Unfortunately, because the interferometer's image was refreshed on-screen at less than 100Hz, blurring merely occurred whenever the driving frequency was not a multiple of the refresh frequency.

Finally we investigate some data obtained from the profilometer testing of a bi-layer SiN_x/SiO_x (approximately 2μm/0.3μm) beam. Results are presented simply in terms of the effective EI of the beam. Initial curvature was eliminated by subtracting pairs of consecutive traces taken at different loads. As the differential force increases, the extracted modulus falls when applying the three top candidate procedures, 2(b), 3 and 4: we have clearly entered the non-linear deflection regime and a simple polynomial model underestimates the modulus in such a case. It is interesting to note that the resampling method consistently fares even worse than the other two methods at large differential forces. Meanwhile, the uncertainty yielded by the successive rejection method increases with force: this is unsurprising because as the shape of the beam goes further away from a cubic polynomial, outliers will tend to be grosser throughout the procedure, so the change in extracted modulus upon each cycle will probably be larger. These data were obtained with more skill and from a cleaner beam than the set of 20 beams analysed earlier; yet the three extraction methods are still not in close agreement. It

becomes clear that systematic errors in the procedure are probably as significant as the random influence of noise.

Figure 22: Extracted effective bending stiffnesses for a SiN_x/SiO_x beam

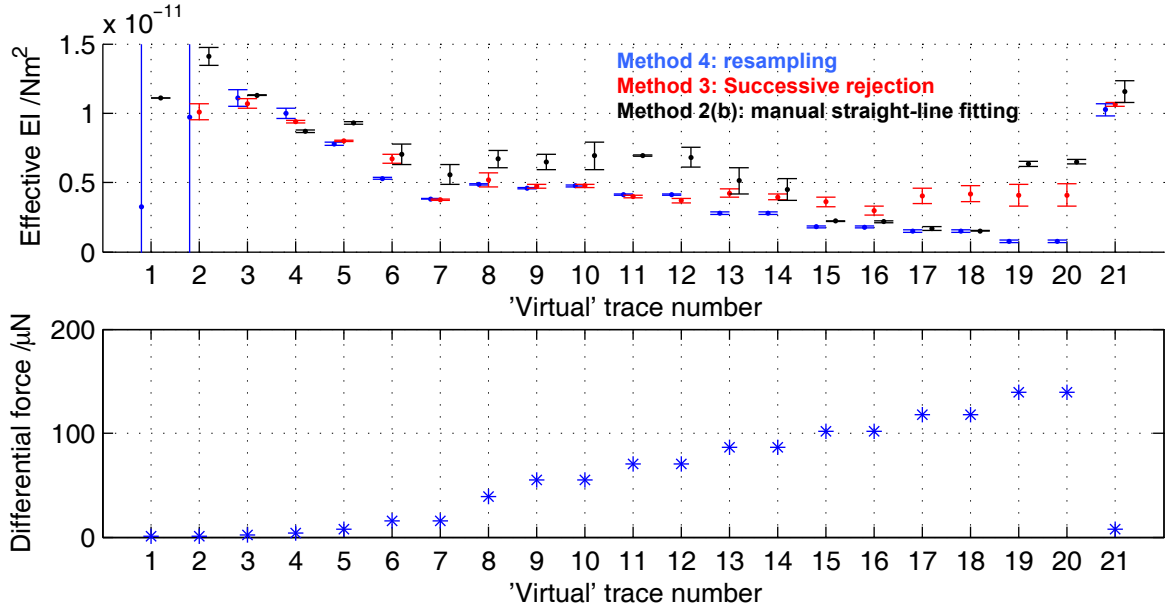

The final differential force applied was a low value equivalent to that used for trace 4 and the similarity of the stiffnesses extracted at the start and end of the run is a good indication that the beam has not deformed plastically or delaminated during testing.

Conclusions

Of the five extraction approaches investigated, none is yet ideal, but the two most promising are (i) the successive rejection of outliers during a series of polynomial fits to the data, and (ii) manually selecting a best-fit straight line on a plot of x–$z^{1/3}$. For the successive rejection method applied to data from the test site designed, the uncertainty in the extracted modulus is typically at least 17%: far above the 10% target. Noise in profilometer traces from dirt on the film and vibration of the beams contributes a large proportion of this uncertainty. However, systematic errors arising from subtle effects not modelled by the extraction procedure — particularly anticlastic curvature — also have a large impact on the accuracy of this test site.

The design of the test site focussed on making it easy to use, but, in estimating the effects of anticlastic curvature, neglected the increase in modulus near the root. We are therefore overestimating E more than originally thought. It is difficult to design a structure that acts perfectly as a beam, but much easier to design one that acts as a plate. This leads to the idea that we should try instead to measure the *plate* modulus of thin films. Indeed, thin-film MEMS designs are more likely to use plate-like components than long, narrow beams; so measuring the plate modulus would probably be more useful than Young's modulus.

More careful processing and cleaning of the devices and better training of the profilometer operator would reduce noise in the traces and misalignments of the profilometer with the sample, improving results at the expense of making the human tester's duties more onerous. The introduction of alignment marks on the test site would allow the stylus's orientation to be determined from the data, and torsion to be compensated to some extent.

A better understanding is needed of the errors in the applied stylus force. If it emerges that the error varies systematically with stylus deflection, we would expect significant problems with the final modulus extracted: as we saw above, any deviation of the trace from a simple polynomial can have a disproportionate impact on the result.

4. Micropackaging concepts

Having investigated ways of measuring the stiffnesses of thin films and processing them to make prototypes, we now move on to apply that knowledge to micropackaging. In the introductory section, the requirements of MOEMS packaging were abstracted and the conclusions drawn now lead to the specification shown in Table 7. The central challenge is that while sub-micron precision is required of the components' final positions, the components are typically several hundred microns in diameter and, if cost is to be reasonable, have dimensional tolerances of about 10%. Any devices that manipulate these components will need careful design to deliver precision under such a range of conditions. Although some researchers have tried to circumvent these problems by building the components into the chip during processing, we consider here the cases where that proves not to be possible.

The device area consumed by any in-built packaging will be significant in determining the costs of MOEMS, but aggressive area minimisation may not be necessary because optical benches often dedicate large proportions of their area to holding fibres in place, and we can consider using the area under those fibres to house packaging devices for adjacent lenses or mirrors [Qinetiq]. Restrictions on the electrical power consumed are less important because we are considering devices that will probably be actuated only once: during assembly.

Rather than addressing one particular optical microsystem, it is the aim of this work to develop technology that can readily be applied to packaging many different MOEMS. The concept matrix in Table 8 summarises ideas considered after surveying the literature, talking to colleagues, and brainstorming.

It was decided to give experimental priority to the first concept — thermal bimorphs made from thin-film beams — because it offers the most opportunities to explore the knowledge obtained in the previous sections.

Table 7: Specification for MOEMS packaging technology

Topic	Requirement (Demand / Wish)	Key word
Function	The technology should be suited to aligning two components relative to one another with precision in up to three angular and two linear axes or vice versa.	Versatility
	The technology should allow for permanent fixing of components in place after alignment, without the need for power to be constantly supplied.	Permanence
Kinematics	The fibre-fibre alignment achieved during assembly should be better than 0.5˚ or 0.7 µm. [Mickelson]	Precision
	The technology should accommodate submillimetre optical components with 10% tolerance of their linear dimensions.	Slop
Forces	Devices using the technology should survive a peak acceleration of up to 10g without leaving the stated bounds on precision.	Shock resistance
	Devices should withstand external vibrations at frequencies from DC to 100kHz and with amplitude 100 µm without leaving the stated bounds on precision.	Vibration damping
Energy	The power consumed when manipulating any one component should not exceed 0.5W.	Max. power
	The stated bounds on precision should not be departed from for a temperature change, outside the device, of 150K.	Temperature range
Economics	Any *additional* device area allocated per optical component to the manipulation technology should not be more than 50% of that conventionally allocated to the component itself.	Area penalty
	The alignment and fixing process should not take more than 10 s per component.	Assembly time
	The technology should be suited to rapid prototyping, preferably allowing any design iteration to be completed within two weeks.	Rapid prototyping

Table 8: MOEMS concept matrix

Function	Solution principles				
Move component to chip	By hand	Pick-and-place robot (cheaper than nano-manipulator)	Sprinkle components over whole wafer; specially shaped 'sockets' on chips would accept components only where they should go; the surplus would brush off.	Don't use discrete components: build them into the chip (e.g. deposit chromium for reflectors and inflate polythene microballoons with transparent fluid for lenses)	
Deposit in right part of chip	Tapered channels to guide components into place				
Manipulate components	Resistive heating and actuators based on differential thermal expansion	Micromachined slots across silicon beams promote folding when compressed, giving an out-of-plane hinge.	Raise a ball by contracting the diameter of its support	Vary the direction of a magnetic field externally applied to magnetically permeable clips (e.g. mix iron powder into polyimide beams)	Inflatable microballoons (forming legs of a tripod) or inflatable clips pressing sideways against components
Check coupling	Built-in test: integral light sources controlled by test circuits		Use precisely-machined stops for critical dimensions.	Sacrifice parallel assembly and use external test equipment	
Fix permanently	UV-hardening epoxy glue.	Engagement of ratchet teeth	Bistable clamps	Resistive heating melts manipulation device, which is fixed when it solidifies.	Inflation fluid hardens after a certain time
Resist external disturbances	Design beams to be as stiff as possible	Choose materials with high elastic modulus and low thermal expansivity when other considerations allow.		Use inflation fluid with low Q when solidified.	

Surface micromachining of e.g. Si_3N_4/Si to form cantilever beams for µclips. Active manipulation of components is possible by making two-layer beams and heating them electrically.

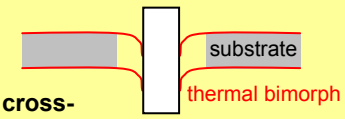

Use a reactive ion etch process to pattern a one-layer silicon-on-insulator structure and obtain out-of-plane motion via compression and buckling.

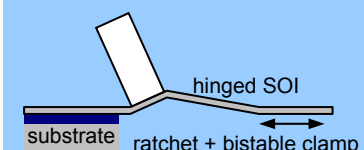

Explore the possibilities of making inflatable microballoons from elastic films, either welded together or spun on to a rigid substrate.

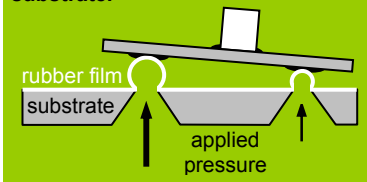

5. Active microclip design

The first micro-packaging concept that we consider involves the patterning of a double layer of thin films to produce electrically heated out-of-plane thermal actuators. These 'clips' would be used in silicon optical benches to position inserted components with the required precision before they were glued permanently in place. A proposed configuration is illustrated in Figure 23. After patterning clips on both sides of a substrate, the material between them would be etched away and a component could be inserted into the gap. The concept's compactness and likely processing simplicity make it attractive for mass-produced MOEMS. Moreover, it is probable that this process would be easier to integrate with CMOS than the concepts discussed in Sections 6 and 7.

Figure 23: Proposed microclip design

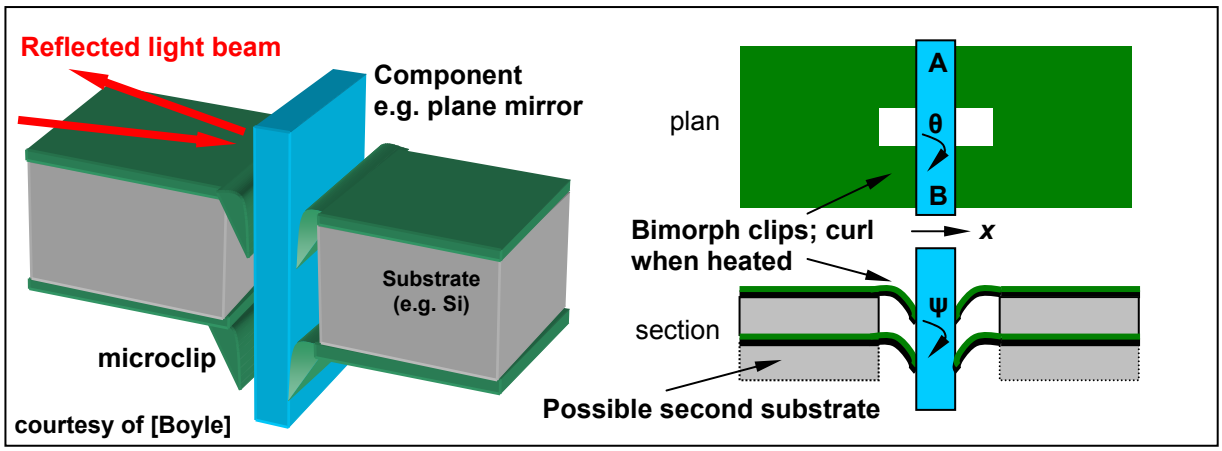

[Boyle] describes work done in this Department to model *single*-layer thin-film clips and finds that typical processing variations would too frequently lead to components being held in positions outside the specifications derived in Section 1. The development of actively controllable devices would allow us to counteract those variations and achieve precise alignment. When manipulating a plane mirror, for example, one linear and one angular degree of freedom, θ and x, must be provided in the plane of the substrate, while one out-of-plane degree of freedom is needed: ψ (see Section 1).

Previous work

Active microclips *per se* are a new concept [Moore2], but much work has been done on thermal micro-actuators. Thermal actuation is more attractive for this application than electrostatic, piezoelectric or magnetic actuation because a greater power density is readily achievable and it should therefore be possible for the clips to offer significant holding forces

at the same time as moving the components. Extensive work has been done on *in*-plane surface micromachined actuators ([Geisberger], [Syms]) and some successful *out*-of-plane bimorphs are reported by [Zhang] and [Gaspar]. [Chen] uses a more complex series of photolithographic steps to deposit two stacked beams, one wider than the other. In this section we prefer to exploit the difference in thermal expansivity between two *different* materials because, for a given power input, greater deflections will be possible than by relying simply on 'hot' and 'cold' arms made of a single material.

Detailed design

Referring to Figure 23, it can intuitively be seen that motion in ψ may be obtained by heating just one of the clips. Motion in θ will happen if the x co-ordinates of the two ends of the component, A and B, change in different directions. Motion in x requires the two clips on one side of the component to push in tandem. If the two films were deposited sequentially on both sides of a substrate, the bimorphs on the bottom would curl in the opposite sense from those on the top when heated. It is not easy to see how such a configuration could provide motion in x. If the order of deposition cannot be changed, it may therefore be necessary to deposit the two levels of clips on separate substrates and bond them later. We will assume for the rest of this section that all the clips will curl in the same sense if heated.

The clips must deflect enough, for a reasonable electrical input power, to move the component from a starting position determined by fabrication imperfections to a position within 0.5˚ and 0.7μm of the ideal. The holding force must be enough to stop the component from slipping through the clips under its own weight. In fact the holding force should be as large as possible to resist any inertial forces exerted by the component if the device is shaken during assembly.

Central to the design process is the expression given by [Timoshenko] for the curvature of a bi-layer beam in terms of its materials' properties and thicknesses and the size of the temperature increase. Where the thicknesses are a_1 and a_2, $a_1/a_2 = m$, the thermal expansivities are α_1 and α_2, the ratio of moduli E_1/E_2 is n, the increase in temperature is ΔT and $a_1 + a_2 = t$, the change in curvature is given by:

$$\kappa = \frac{6(\alpha_2 - \alpha_1)\Delta T(1+m)^2}{t\left[3(1+m)^2 + (1+mn)\left(m^2 + \frac{1}{mn}\right)\right]} \qquad \ldots 2$$

To maximise motion for a given temperature increase we therefore want to maximise $(\alpha_1 - \alpha_2)$ and minimise t. The ratios (a_1/a_2) and (E_1/E_2) have subtle effects and will be ignored

during the initial materials selection. An analysis given by [Han] implies that, provided that $a_1 \approx a_2$, such an approximation is reasonable. The other key model governing the design is one relating a clip's deflected geometry to its tip force and maximum bending moment. In analysing passive clips, [Boyle] computed the deflected shapes of such clips, resulting in the graphs of normalised elastic potential energy and holding force shown in Figure 24.

Figure 24: Graphs of clip behaviour normalised by bending stiffness

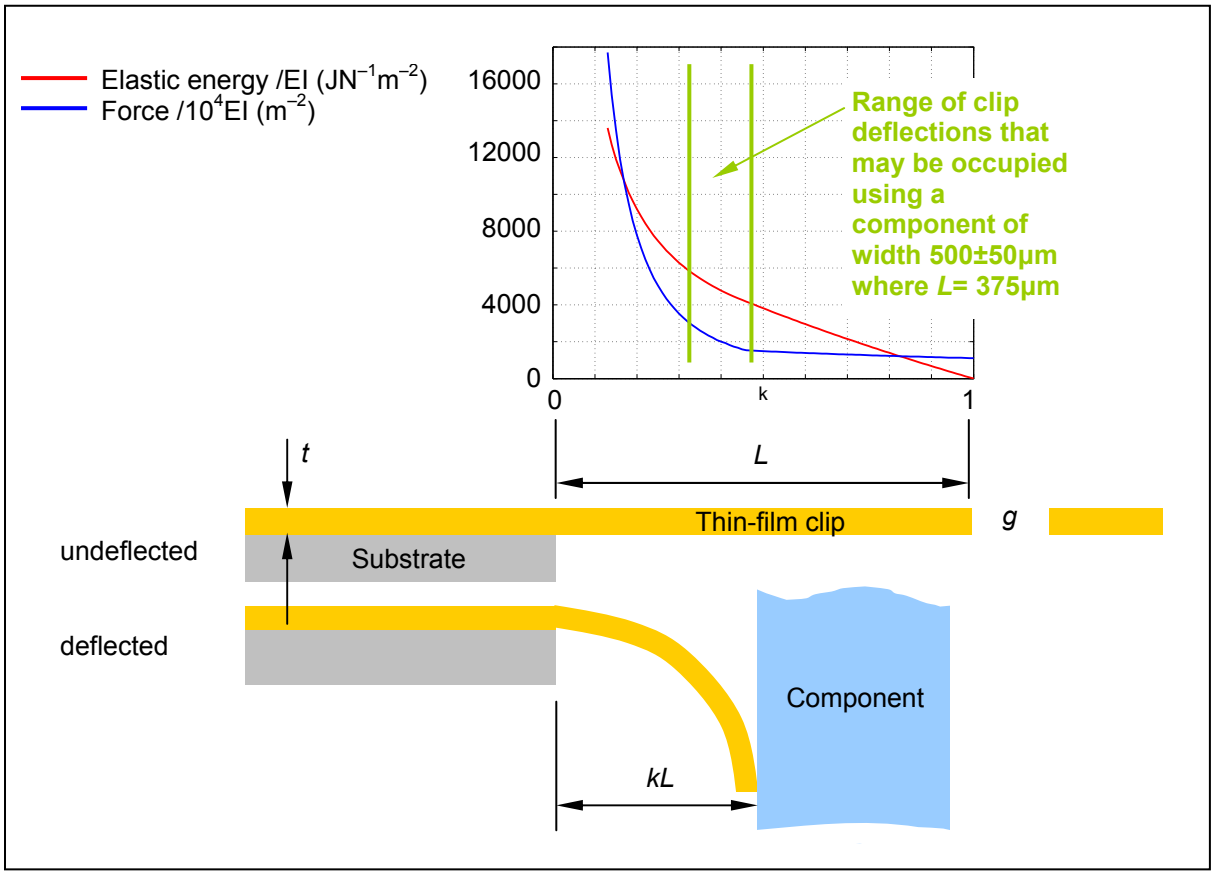

The design now divides into two parts: choosing the materials and their deposition thicknesses, and designing the in-plane clip geometry. The process can be stated as:

1. Choose pairs of materials with large differences between their thermal expansion coefficients.
2. From pairs of materials with similar expansivity differences, choose preferentially those with the greatest average Young's modulus, so as to maximise holding force.
3. Guess film thicknesses and clip length to satisfy the deposition capabilities of the chosen materials, the modulus of rupture of the materials, and the demands on tip manipulability, holding force and shock resistance.
4. Check the design by simulation. Iterate through steps 3 and 4 until a satisfactory solution is found for each pair of materials or it is decided to reject a pair.

Table 9 below summarises the conflicts that exist in the design process:

Table 9: Conflicting aims in the design of microclips

Parameter	Aim 1: maximise tip deflection per unit temperature change	Aim 2: maximise holding force and therefore shock resistance
α (thermal expansivity)	Maximise difference between the two materials	–
E	Ratio of E has weak effect on thermal curvature; neglect in initial design	Maximise so that preference can be given to longer clip lengths in the trade-off below
t	Minimise [Timoshenko]	Maximise to increase bending stiffness of clip
L (clip length)	Maximise to maximise tip displacement	Minimise to increase curvature in clip and hence holding force
g (gap between clip tips when undeflected)	–	Minimise so elastic energy stored in clip is maximised

Choosing materials. We must obviously restrict ourselves to those polymers, metals and ceramics that can be deposited as thin films. In general, polymers and metals would be considered for the upper (more expansive) material and a ceramic for the lower one, but there are some polymer–metal and even ceramic–ceramic combinations that might work. Table 10 below suggests combinations and evaluates their average Young's moduli and the differences between their expansion coefficients. Where neither material is electrically conductive, a non-structural heating element would be added. The functional resist SU-8 and the widely used MEMS polymer PDMS are assumed to have thermal expansivities of $70 \cdot 10^{-6}$ K^{-1} and moduli of 4GPa, like PMMA.

Table 10: Candidate material combinations for bimorphs. Each cell is in the format (differences in α /10^{-6} K^{-1}) / (geometric mean of E/GPa). Most data is from [Ashby] p45.

Layer 1 (lower) ▼	Layer 2 (upper) ▼							
	SU8 or PDMS	Al	Cu	Ni	Ti	Mg	Cr	ta-C
Al	50/10	-	-	-	-	-	-	-
Cu	50/10	-	-	-	-	-	-	-
Ni	55/10	-	-	-	-	-	-	-
SiN	67/20	17/150	17/200	12/200	6/200	27/100	2/300	2/600
Al_2O_3	61/20	11/200	11/200	6/200	0/200	21/100	–4/300	8/600
SiC	66/20	16/200	16/200	11/250	4/250	26/150	0/300	3/700
ta-C	70/20	19/300	19/300	14/400	8/300	29/200	4/600	-
SiO_2	70/20	19/80	19/100	14/100	8/100	29/60	4/200	0.4/300

The performances of most metal-on-ceramic combinations seem very similar; however a thermal expansion difference three to four times greater seems possible with a polymer–ceramic or polymer–metal combination, at the expense of a significant fall in

average modulus. A combination of particular interest is SU-8/ta-C, although the large residual compressive stress commonly encountered with ta-C would need to be overcome first. Magnesium is of interest, with its rather higher thermal expansion coefficient than, say, aluminium, but is too highly reactive. Mg/Al alloys might be considered instead. The yellow-highlighted combinations are the most attractive, but for the purpose of making initial prototypes it has proved convenient to try the two combinations shown in green. We gain encouragement for some of these conclusions from the literature, which reports bimorphs made from Ni/diamond [Schmid], Al/Si, Cu/SiO_2 and W/SiO_2 [Zhang]. No bimorphs involving SiN have, to my knowledge, been reported; so the results from these prototypes could be interesting.

Other factors that will be important are fracture toughness, cost, ease of processing, and the propensity of a given combination of films to delaminate.

Choosing clip dimensions. The width of the microclip does not feature in Equation 2 and so is irrelevant in attempting to maximise thermal deflection; meanwhile the holding force will be maximised by deflecting as much clip material as possible. This implies that clips should be rectangular: there is no point in removing more of the deposited films than absolutely necessary.

Given a free choice between many narrow clips and few wide ones, it is slightly better to choose a few wide ones, firstly because less material is wasted by the gaps between clips and secondly because the clips will resemble plates and will be stiffer than narrow beams per volume of material by a factor of up to $1/(1-\nu^2)$. Subdivision of clips is necessary, however, to ensure that the etching of the silicon substrate beneath them can proceed at a suitable rate. Subdivision of clips also allows us to use the shapes of the clips to define a current path for electrical heating.

It makes sense to start with the films as thin as possible: this will maximise thermal deflection and minimise longitudinal stresses at the root, although very thin clips may not offer enough holding force. The clip length L and gap g then need to be chosen by weighing up the requirement for a large holding force (a short clip is needed) against that for a large thermal deflection (a long clip is needed so that a given curvature leads to more tip movement).

A typical component to be accommodated [Etalon] has thickness 500±50μm and a side length about 2mm. Figure 24 shows that a rectangular clip begins to be pushed flat against the component when confined in a space 0.4 times as long as when unbent. A flat region in the clip stops thermal curvature from having its full effect but leads to much larger

contact forces, so a suitable compromise would seem to be to design the clip length so that it is *just* beginning to be pushed flat against the component when the component is inserted. For a component half-thickness of 250µm and g = 25µm, a clip length of 375µm is implied.

It is straightforward to predict the electrical resistance of the designed clip but extremely challenging to model the heat dissipation from the clip in a way that would tell us how electrical power input is related to the resulting thermal curvature. Such analysis will be left for later prototypes.

Figure 25: Possible equilibrium configurations of clips: (a) normal; (b) unwanted local energy minimum

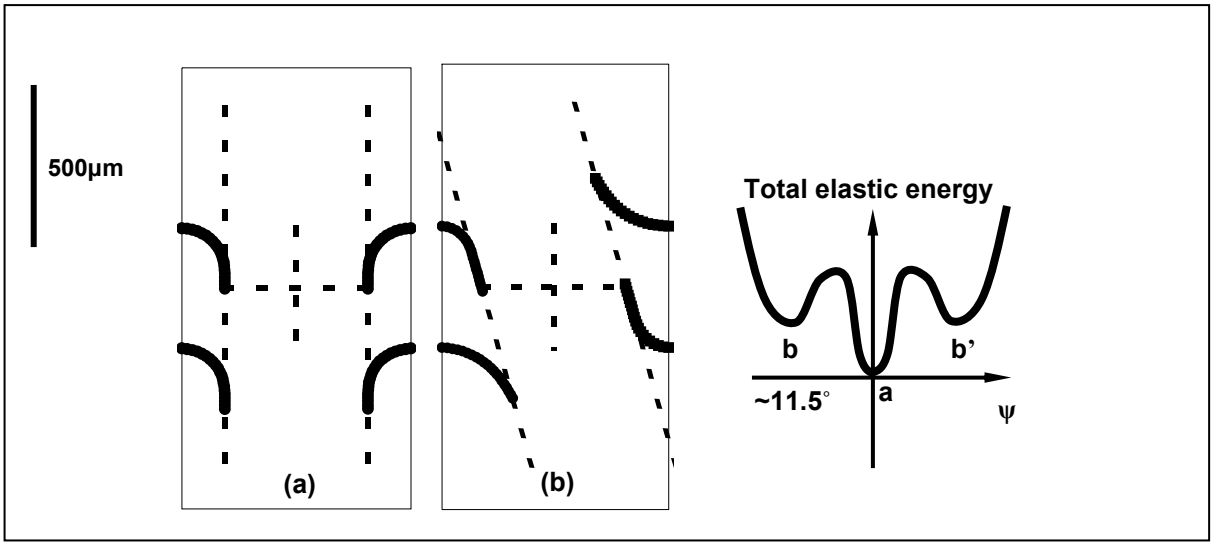

Simulation

The main purpose of simulating the chosen geometry is to establish the relationship between temperature increases in the clips and the orientation of the component. We also want to check the maximum stresses at the faces of the clips and at the interfaces of the two layers.

[Boyle] achieved the graphs in Figure 24 by using Microsoft Excel with a plug-in constraint solver to find the equilibrium shape of a grossly deflected clip. He found the shape corresponding to a minimum in the total elastic energy stored in the clip. The clip was modelled as a string of torsional springs joined by rigid bars. By running a sequence of energy minimisations in which the constrained position of the clip's tip was gradually varied, an energy–position relation was obtained and its spatial derivative gave the force–deflection relation.

For this work I have devised a way of extending the approach. At each torsional spring in the model, the curvatures due to elastic deformation and electrothermal actuation are superimposed. The energy objective function, however, considers only the deformation due to elastic bending. Energy minimisation is now performed on four clips simultaneously, representing a cross-section through a micro-package. The clips' tip position constraints are

linked by a model of the component as a rigid rectangle that can move in ψ and x. Equilibrium occurs when the sum of elastic energies in *all* the clips is minimised, and thus the resting orientation of the component, subject to any given processing misalignments and clip temperatures, is automatically found.

Figure 26: Counteracting misalignments by heating clips

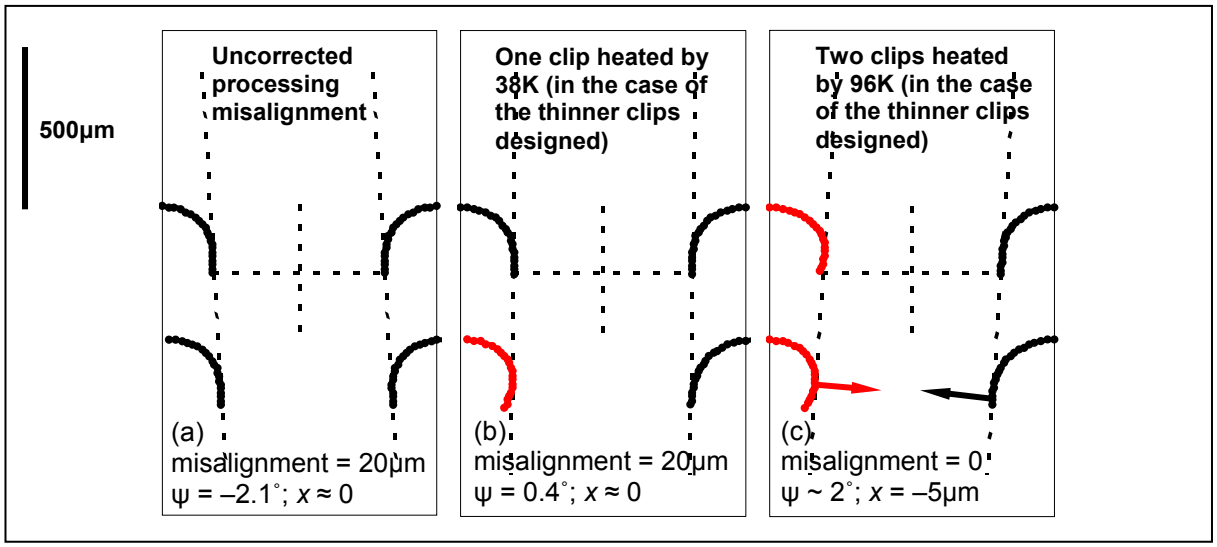

Starting with the situation where the two layers of clips are perfectly aligned, Figure 25(a) shows that the clips would be pressed slightly flat against the component. Figure 25(b), however, shows an unwanted configuration corresponding to a local energy minimum, which might occur if the component were inserted obliquely or the assembly were vigorously shaken. Making the distance between the clips' roots as small as possible raises the energy barrier to our entering such a configuration. Assuming a 600µm substrate, if a (rather pessimistic) 20µm front-back misalignment were to occur, the component would rotate by about 2˚ (Figure 26(a)). By heating the clip shown in red in Figure 26(b), the unwanted rotation can be compensated. If motion of the component in x is required, both the red clips in Figure 26(c) would be heated: motion of 5µm is achievable according to this simulation. Because the line of action of the contact forces (shown by arrows in Figure 26(c)) moves away from horizontal as the clips are curled by heating, the component rotates as well as translating. Consequently the relationship between clip input power and component orientation will be a complex one.

Now that we have established the geometrical changes that are needed to counteract misalignments, we can simply scale the results to obtain, for any pair of films, the required input temperature change (by applying Equation 2), and the resulting stresses (by calculating a clip's effective bending stiffness and applying simple structural mechanics based on the simulated root curvature). The clip *length* must of course stay the same for this scaling to be

possible. Simulation results for the two designs that have been prototyped are summarised in Table 11 below.

Table 11: Microclip simulation results

Material combination	Chromium/SiN[TM]	Copper/SiN[Nortel]
Thicknesses /μm	0.9/2.4	0.45/0.14
approximate Young's moduli /GPa	279/200	130/200
Thermal expansivities /10^{-6} K^{-1}	4.9/1.6	16.5/1.6
Notional rupture moduli /MPa	60/300	60/300
Stress at top surface, root /MPa (tension +ve)	3130	305
Stress at bottom surface, root /MPa	–2580	–395
Stress at interface, upper material /MPa	1290	–123
Stress at interface, lower material /MPa	926	–190
Effective *EI* per unit width /Nm	6.96 10^{-7}	2.68 10^{-9}
($d\kappa/dT$) /$m^{-1}K^{-1}$	1.3	31.0
Temperature increase required in one clip to rectify a 20μm misalignment /K	920	38
Temperature increase required in two clips to cause a 5μm motion in *x*.	2290	96
Approximate holding force *H* applied by each clip per unit width (from Figure 24) /Nm^{-1}	13.9	0.054

It is apparent that the first design, with a total clip thickness of 3.3μm, would experience bending stresses far in excess of the materials' strengths. The stresses in the other design, 0.59μm thick, are much lower but would still lead to failure. Meanwhile, the temperature increases required by the thicker clip are enormous and trying to move a component 5μm in *x* would consume huge power and cause the chromium to melt. To prevent slipping under gravity the holding force *H* should at the very least satisfy the relation $2\mu H > (W/2)$ where μ is the coefficient of friction between clip and component and *W* is the weight of the component — about 50μN. Estimating μ to be 0.2, we require $H > 63\mu N$ over the 2mm component width, or $0.03 Nm^{-1}$. In practice we would like a much larger force. The simulated holding forces both exceed this lower limit but the thicker clips would offer far superior shock resistance.

A change in design will therefore be necessary to make the proposed basic configuration work. To reduce peak bending stresses we could reduce the thickness or increase the length at the expense of reducing holding force. Another way to proceed is to consider that the peak bending stress σ is proportional to Et, whereas the holding force is proportional to Et^3. We therefore find that if we choose materials with higher (σ_f^3/E^2), where σ_f is the maximum stress of the material, we are able to increase the holding force for a given clip length, although at the expense of a thicker clip and hence a smaller ($d\kappa/dT$). This analysis is obviously complicated by the need to choose a *pair* of materials. [Ashby] shows on p88 that ceramics such as SiN_x actually have among the highest (σ_f^3/E^2), but that the metal

part of the proposed bimorphs might usefully be replaced by an elastomer such as spun-on silicone rubber. SU-8 could also be considered.

It was decided to proceed with prototypes of the designs simulated, however, to gain an insight into any challenges in fabrication not identified by the simple model so far used.

Experimental results and discussion

Figure 27 shows the designs that were manufactured. The design shown in (a) was patterned on a bi-layer of 0.45μm copper sputtered on to 0.14μm LPCVD SiN_x/Si supplied by Nortel (c). The beams were then under-etched in 25% KOH:H_2O solution at 80˚C for approximately 90 minutes, removing the silicon beneath the beams but leaving support under the large contact pads. The sputtered copper appears to have been under residual compression because a majority of the cantilevers curled downwards by about 100μm when released: (d) shows the beams bending out of a micrograph's depth of focus.

Two sets of the cantilevers shown in Figure 27(b) were made. For one set, the design was laser-patterned on to a sample of 2.4μm LPCVD SiN_x[TM]/Si and under-etched *before* sputtering with about 0.9μm Cr. For the other set, the Cr was deposited before the laser patterning and etching. Again, residual compressive stress in the Cr was obvious: all beams curled down.

All three sets of bimorphs were tested by applying a gradually increasing potential difference across each pair of pads in turn. The tests were performed under an optical microscope and vertical deflection was measured by determining the change in objective position needed to keep the beam tip in focus. This method is imprecise, with an estimated uncertainty of ±5μm. The beams were tested to destruction and the mode of failure was noted: it was typical (as shown in Figure 27(e)) for the metal to oxidise over a period of ~10 seconds, leaving the bimorph discoloured before it snapped about half way along the beam, where the temperature was presumably at its highest. Some beams fractured instead near the root, implying that a crack introduced there during manufacture had propagated. An exploratory prototype made much earlier from Ni/SiN showed that, around the crack, the metal had also melted, but it was not clear which material had failed first.

Two additional bimorphs of the same size were fabricated on the Cu/SiN sample with tip supports that were removed by laser ablation after under-etching. This precaution was taken in case the unsupported cantilever beams were broken by stiction during the after-etch dry.

Figure 27: Prototype bimorphs: (a) laser design for Cu/SiN[Nortel] clip array (dimensions in mm); (b) laser design for Cr/SiN[TM] bimorph array; (c) optical micrograph after laser cutting of pattern but before etching in KOH; (d) three Cu/SiN bimorphs after release; (e) single Cr/SiN bimorph after testing

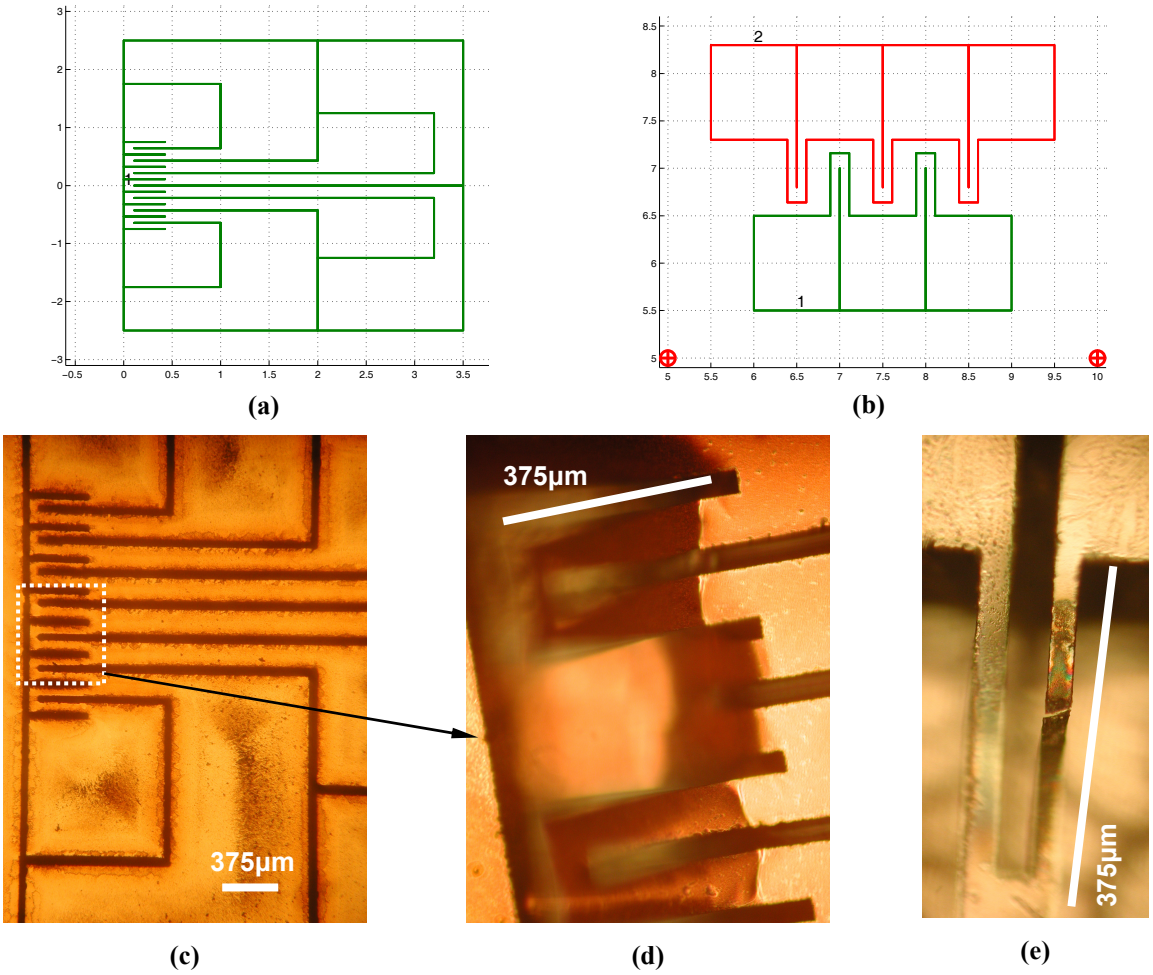

(a) (b)

(c) (d) (e)

The yield of usable results was poor: some of the bimorphs failed before any deflection was discernible. Figure 28 summarises the voltage (V), current (I) and vertical deflection (z) measurements that were obtained, reduced to a power–curvature graph on the basis that $P = VI$ and $\kappa = 2z/L^2$ where L is the beam length. The latter relation assumes that deflections are small but since deflections started in excess of 100µm because of the residual compression in the metal, this analysis must be taken as crude.

Looking at Table 12 first, the predictions of the bimorphs' resistances greatly underestimate the measured values. This may be because the contact resistance between probe and metal film was significant, because the films were both thinner than the values assumed, or because the films were porous or cracked. The bimorphs made by sputtering after patterning had significantly lower resistances: so much lower in fact that not only must the chromium have coated the edges of the cantilevers; it must have coated to an extent underneath the beams as well. This is to be expected since sputtering is not typically a strongly directional process. We know the basic Cr thicknesses are identical because both

samples were coated in the same sputtering cycle. Those bimorphs tested six weeks after the others appeared to have very much larger resistances, perhaps because the film had oxidised, making electrical contact harder.

Figure 28: Experimental results reduced to curvature-power relationship

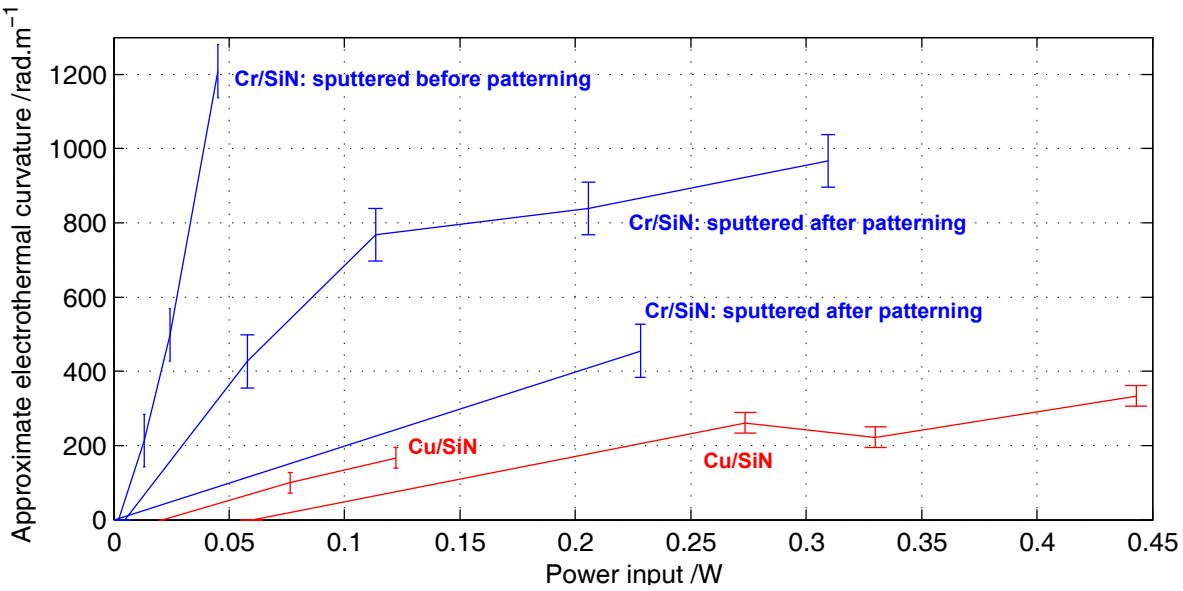

The observations made about the order of fabrication are supported by Figure 28. The Cr/SiN bimorph that could *not* have been coated on its edges or lower face deflected much more than the others for a given power input; the beams with at least some metal on each face operated less efficiently. The two processing flows were tried to check whether it would be possible to laser-ablate only the thin layer of SiN and add the metal later, speeding up the micromachining process. If evaporated aluminium were used as the coating, however, the conclusion would indeed be to pattern, then deposit: evaporation is directional and Al etches in KOH.

Table 12: Comparison of predicted and measured bimorph resistances

Design	Number of 'squares' in beam	Predicted resistance /Ω	Measured resistances /Ω
Cu/SiN[Nortel]	12.12 (including 0.56 per corner)	0.5	7.7, 5.5, 2.9
Cr/SiN[TM]		1.7	9.9, 5.5, 7.9, 5.9, 6.9 (sputter then pattern) 2.8, 4.5, 3.2, 16*, 26* (pattern then sputter) * six weeks later

The very much thinner Cu/SiN beams deflected less for a given power than the Cr/SiN ones. This outcome is surprising because the predicted ($d\kappa/dT$) of the thinner beams was about 24 times larger (Table 11). It is possible that heat conduction to the substrate was greater with the Cu/SiN beams: the etch pit in the Si was rather shallower.

One of the Cr/SiN traces seems to show a flattening off at higher powers. It is not, however, possible to conclude, as one might be tempted, that this means radiative power losses are becoming significant: the beam may simply have hit the bottom of the etch pit.

Conclusions and future proposals

The bimorphs fabricated in this section show an encouraging amount of electrically-actuated curvature, especially those made from 0.9μm Cr on 2.4μm LPCVD SiN. The power consumption is of a suitable order but perhaps in need of reduction when we consider the requirement of the specification for *all* the devices used in manipulating a component to take no more than 0.5W in total.

Yield of these first-stage prototypes has been poor and little progress has been made on producing clips on both sides of a substrate. A way of micromachining the materials with smoother edges would probably increase yield: some early failures seem to have arisen from the propagation of an edge crack. The beam roots should be rounded to prevent brittle fracture there. Photolithographic patterns have therefore been developed featuring arrays of clips.

The accuracy of future measurements could be improved by actuating the bimorphs with an AC signal and using a laser Doppler vibrometer to measure the amplitude of vibration. Such an approach would also identify any unwanted resonances of the design, and would allow us to test for fatigue.

The main failing of the design as it stands is the inability of the clips to be bent through large deflections without snapping. To this end, it may be fruitful to develop polymer-on-ceramic bimorphs. Brittleness in the SiN layer has been identified as a problem — the beams snap — so it may be valuable to try making particulate composite films. For example, by sprinkling iron powder into SU-8 before spinning it on, film toughness could be improved at the same time as allowing an externally applied magnetic field to manipulate the clips: a possible simpler alternative to electrical actuation.

The difficulty of selecting suitable materials to give both adequate holding force and thermal curvature may well mean, however, that active microclips prove not to be a successful MOEMS packaging concept. Microclips do, however, hold clear promise as a means of achieving electrical connections at the microscale, perhaps to connect two integrated circuit dies together with minimal parasitic inductance. The holding force need not be as large as for MOEMS packaging, and, because the components would be resting against a firm support, precision of manipulation would not be such a challenge. Indeed, [Zhang] has already reported a MEMS probe card using thermal bimorphs.

6. Silicon-on-insulator out-of-plane packaging

Although the thin-film clips investigated in Section 5 would provide a good solution if the difficulty of choosing materials for them could be overcome, in this section we consider the use of a more expensive, but robust, technology — deep reactive ion etching (DRIE) of silicon — to achieve a similar effect reliably: precise rotation of a component out of the plane of a MOEMS optical bench.

Work in recent years on surface-micromachined mechanisms has divided into two camps: multi-layer processes (e.g. [Sandia]) which achieve sophisticated motion with complex design, and single-layer approaches, which have been limited to in-plane motion. In the latter camp, mechanically bistable designs have been demonstrated [Jensen], as have electrothermally actuated beams [Que, Syms]. Work to combine these two concepts for MOEMS packaging is continuing in this Department [Boyle1], where DRIE of ~60μm-thick silicon-on-insulator (SOI) is used to provide stiff structures capable of supporting MOEMS components. This section presents a proposed modification of the DRIE procedure that will allow out-of-plane motion.

Figure 29: Left: plan and section of device structure; right: half pseudo-rigid body model of device

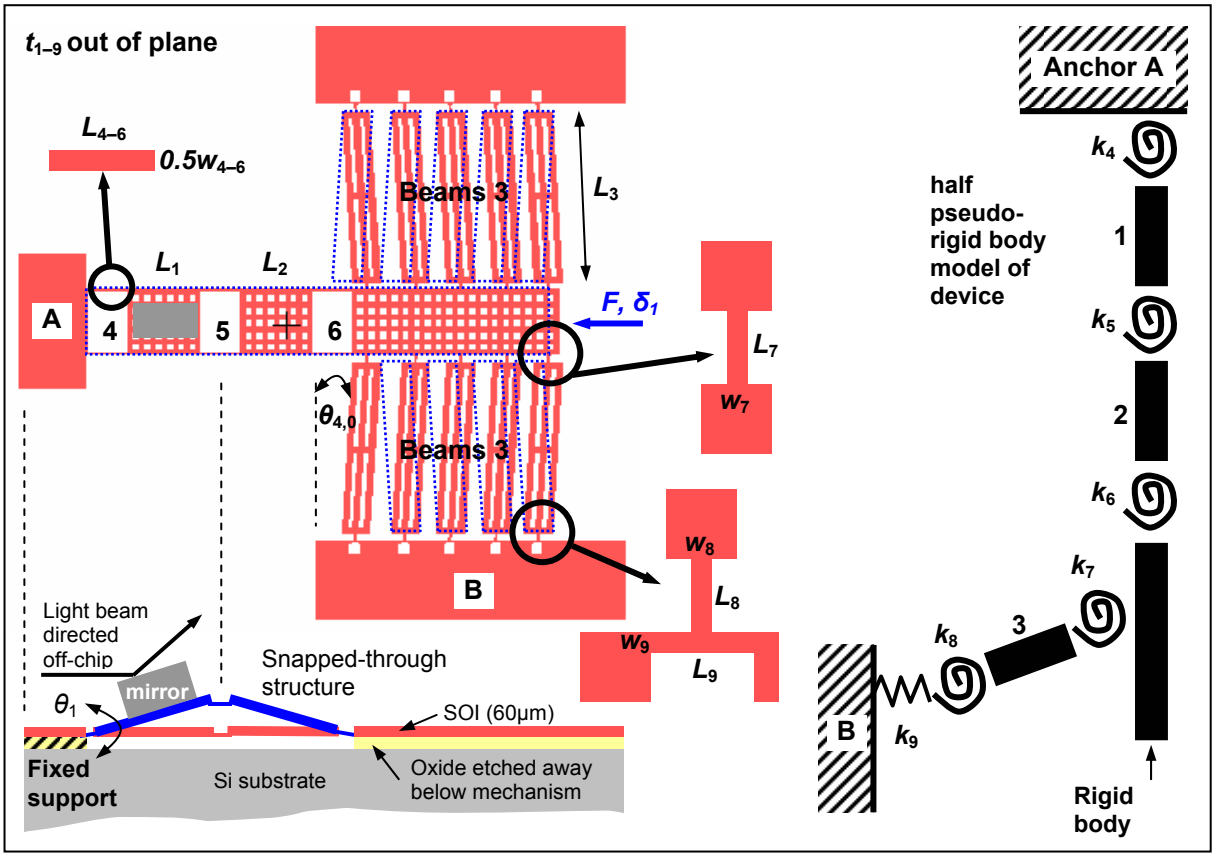

The concept is illustrated in Figure 29. The SOI would be DRIE etched through and the oxide layer etched by buffered HF to release the mechanism. By thinning the SOI layer at points **4**, **5** and **6**, hinges would be formed which prefer to bend out of the plane. A MOEMS component such as a mirror would be glued (with limited precision) on to platform **1** and force F would be applied horizontally to make beams **3** 'snap through' to the dotted position, while a small upwards force on the component would make sure platforms **1** and **2** deflected upwards rather than downwards. The thinning of the hinges could be done by laser ablation (as investigated in Section 2) or by exploiting DRIE 'lag', which causes very narrow features to etch slowly [Ayón].

The component would rest rotated out-of-plane by a few degrees, a potentially useful way to direct light signals from one MOEMS die to another within a system. The component would not, however, be perfectly positioned after simply snapping the device through and final precision could be achieved by electrothermal actuation of beams **3** before gluing the device in place. For this first prototype, however, it was decided to consider the mechanical design alone.

The design is thus reduced to choosing values for $L_{1–3}$, $\theta_{4,0}$, the dimensions of the hinges and the number of beams **3** in parallel. [Jensen] shows that a good approximation is achieved by reducing mechanisms such as this to a 'pseudo-rigid body' model in which beams **1**, **2** and **3** would be stiff and hinges would be modelled either as torsional springs or, in the case of the side flexures **9**, as linear springs. He directly expresses the force applied to a mechanism in terms of its deflections, but, in our case, where we want to consider the effect on the structure of a component with considerable weight, it is easier to express the total energy stored in the system and differentiate it with respect to δ_1 to find $F(\theta_1)$.

The design was performed using Matlab to maximise the force, $–F$, required to collapse the device after it has been snapped up: in other words to maximise the shock resistance of the mechanism. To restrict the computational complexity of the optimisation, the number of beams labelled **3** was fixed at 5 on each side, $w_{7–9}$ were fixed at the technological minimum, 10μm, $L_{1–2}$ were fixed at 1mm, and $L_{7–9}$ were constrained to be equal, as were $L_{4–6}$, $w_{4–6}$ and $t_{4–6}$. This left six crucial variables determining the peak stresses in the hinges and the snap-through force: L_4, L_7, w_4, L_3, $\theta_{4,0}$ and t_4. Generally, the smaller the flexures are, the greater the snap-through force will be, but the higher the bending stresses in the silicon. Since the weight of the component is significant, to hold the stage up either flexures **7**–**9** need to be rather stiff, or more beams **3** can be used in parallel.

Because we want to achieve a certain component rotation, simulations were done in terms of θ_1. The simulation procedure for a given trial set of dimensions was as follows:

1. Calculate spring constants k_i (torsional or linear as required) for all hinges, using simple beam theory: assume deflections to be small.
2. Check that hinges **4–6**, which are supposed to bend out-of-plane, are indeed more compliant in that direction than they are in-plane.
3. Over the full range of θ_1 that is geometrically possible, evaluate the deflections of the hinges, the changes in the vertical position of the component, and the motion δ_1 where F is applied.
4. For each θ_1, sum the gravitational potential energy gained by the component in being lifted up and the elastic energies in the hinges (using $0.5k_i\theta_i^2$ for torsional springs and $0.5k_9\delta_9^2$ for the side flexures).
5. Calculate the maximum stresses in each of the hinges as a function of θ_1. If any stress exceeds a conservative value for the breaking stress of silicon, reject the design.
6. Differentiate the total energy $U(\theta_1)$ with respect to $\delta_1(\theta_1)$ to obtain $F(\theta_1)$. The peak negative value of $F(\theta_1)$ needs to be maximised in magnitude by varying the design's dimensions.

Figure 30: Simulation results for chosen parameters and 100µN component weight

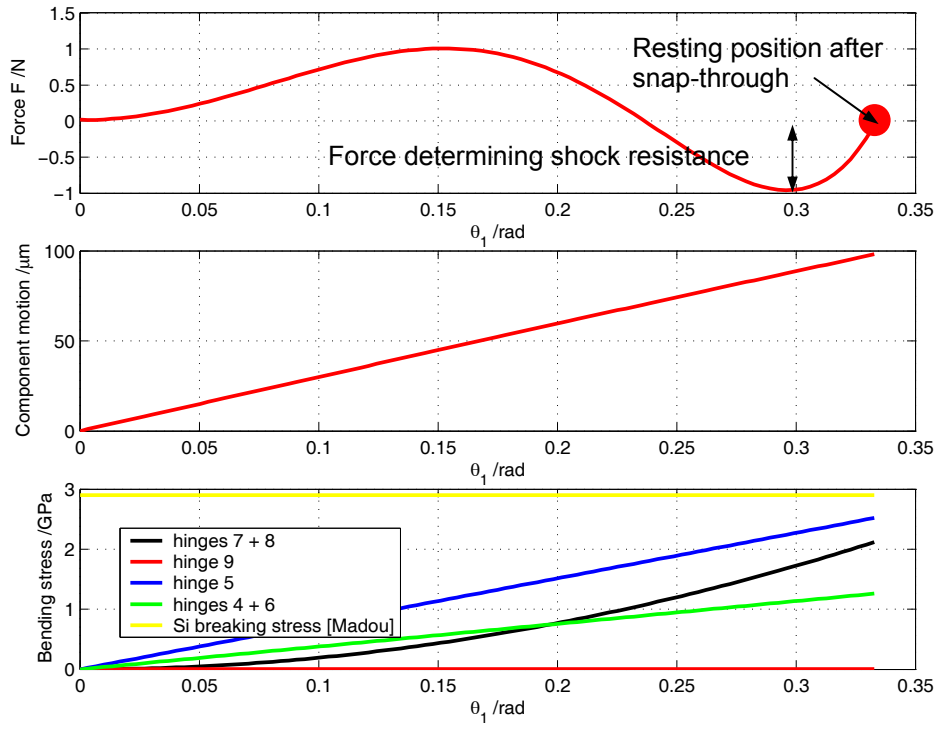

Chosen parameters:

$L_{1-2} = 1000\mu m$
$L_3 = 1400\mu m$
$L_{4-6} = 213\mu m$
$L_{7-9} = 30\mu m$
$w_{4-6} = 43\mu m$
$w_{7-9} = 10\mu m$
$t_{4-6} = 9.8\mu m$
$t_{7-9} = 60\mu m$
$\theta_{4,0} = 0.04$ rad

The results of simulating the chosen design are shown in Figure 30. The chosen design and a range of slight dimensional variants of it were fabricated in SOI at Imperial College. Also included on the mask was an array of slits (Figure 31(d)) with widths from 1µm to

20μm, intended to characterise the DRIE lag of the particular etching 'recipe' used at Imperial. By determining the etched feature depth as a function of slit width, it would be possible to add sets of appropriately narrow slits at the hinge positions of future masks, automatically making the SOI layer thinner on average there. The extra laser ablation step would then be avoided.

A fabricated device is pictured in Figure 31(a), and the result of laser-thinning the SOI layer at a hinge is shown in (b). A reasonably clean finish has been obtained but the final thickness of the hinge, a critical dimension, is hard to check accurately from the image. (c) shows that the release of the mechanism from the substrate has not been completed: small residual islands of unwanted oxide are seen after breaking off the functional layer. Although the design adhered to empirically derived rules — not to make any beam wider than 40μm if it is to be released, and to make etch holes wider than 50μm — some step in the processing on this occasion has led to failure. A longer buffered HF etch could solve the problem; alternatively the widths of the beams could be slightly reduced. So although the design appears promising as a simple way of achieving out-of-plane motion, it has not yet been possible to prove that with a prototype.

Figure 31: scanning electron micrographs of processed device: (a) overall image; (b) laser-thinned hinge after 200 pulses of green radiation each at 7.4 . 10^4 Jm^{-2}; (c) showing unetched oxide sacrificial layer; (d) array of lines to test DRIE lag and cross-section of an idea for hinges exploiting it.

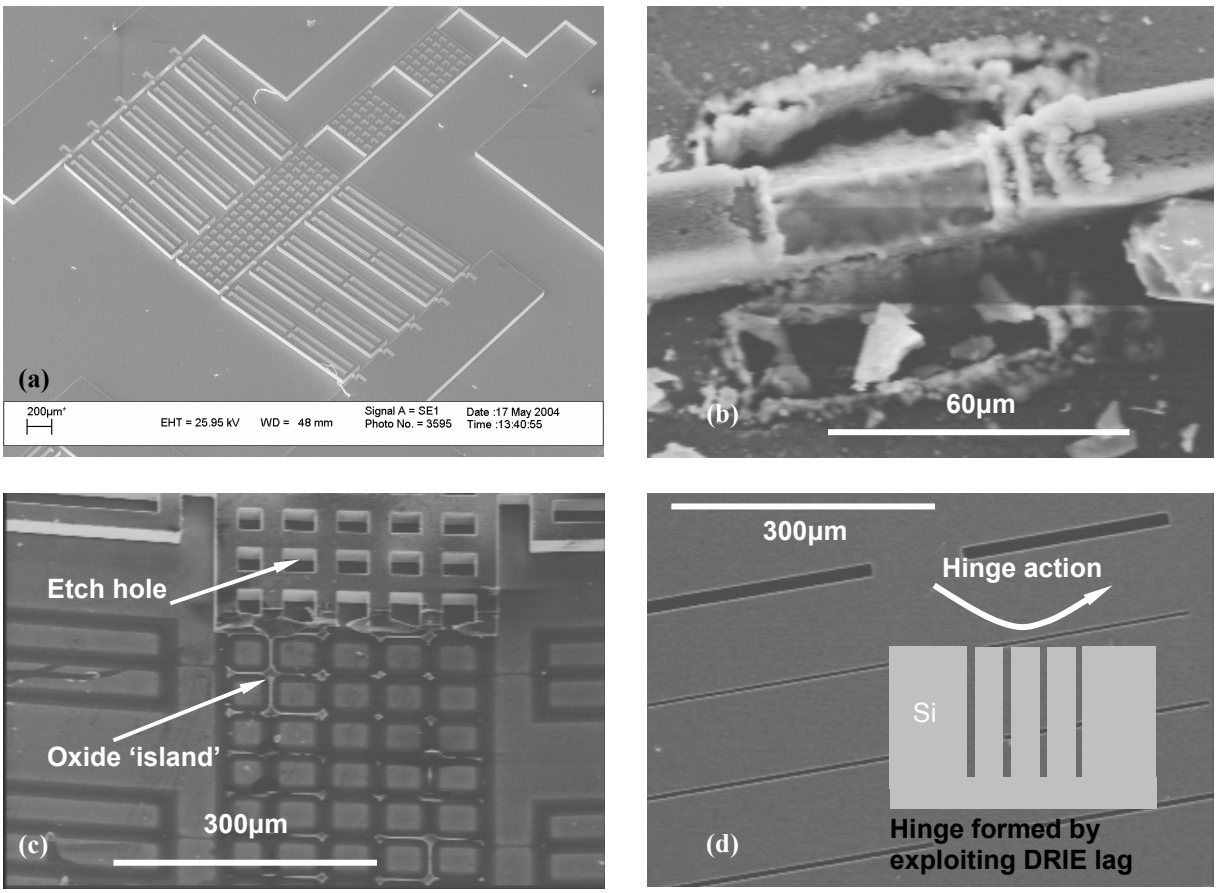

7. Inflatable packaging structures

The primary problem identified with the metal-on-nitride bimorph clips in Section 5 was their propensity to fracture when deflected through the large angles necessary. A very different approach that we might consider instead is to replace electrothermally actuated clips by inflatable ones, and manipulate components by controlling the fluid pressure inside the clips. Such structures could be made by selectively welding together two thermoplastic films and then pumping fluid between them. This approach is attractive for three reasons. Firstly, the welds around the clips would ensure that the main stresses in the clips — arising from the fluid pressure — would not exist right at the edges of the material. This would make the propagation of cracks from the edges of the clips less likely. Secondly, the holding forces of the clips would be larger for an inflated structure than for the same material uninflated. Thirdly, there would be the opportunity to fix components permanently in place by choosing a particular inflating fluid — such as epoxy — that would solidify after enough time had been allowed to position the component accurately.

An attempt to make inflatable clips is shown in Figure 32. A mould was made by laser-ablating a clip pattern in some SiN/Si and etching in 25% KOH solution at 80°C for 3 hours. This mould was then laid on top of two sheets of 20µm-thick polythene and a soldering iron was touched on to the back of the mould for a few seconds. The heat conducted to the polythene led to a weld being formed in the shape of the clips' outlines. The quality of the weld was very sensitive to the heating time, and, as the optical micrograph in Figure 32(d) shows, was typically poor. Nevertheless, further investigation could yet prove fruitful.

Figure 32: Prototyping inflatable microclips: (a) section of concept; (b) prototyping technique tried; (c) diagram of silicon mould; (d) optical micrograph of weld formed in polythene film

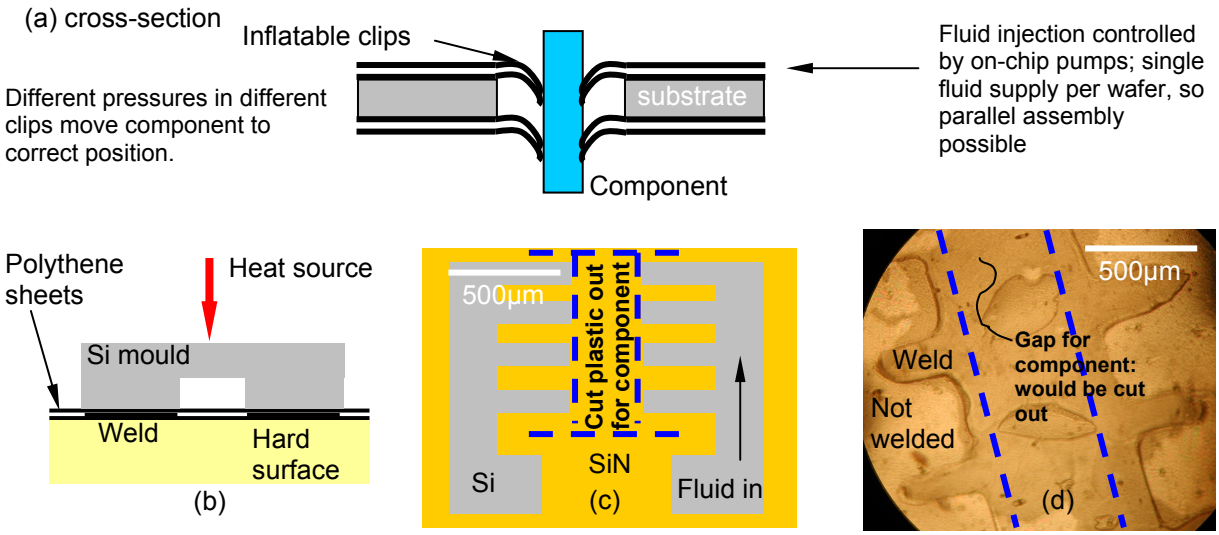

8. Overall conclusions

Each part of the project has been concluded in its own section, but here we review where the work as a whole leaves us. We now have a clear idea of the wavelengths and pulse fluences — generally of order 5–6 . 10^4 Jm^{-2} — that should be used to laser-ablate SiN, SiC, ta-C and metal films cleanly with a ns-pulse length system, and we will be able in future to produce well finished prototypes upon a first attempt. Work on bimorph beams has indicated that, for multiple layers, laser ablation's advantages over photolithography and RIE are accentuated: with a laser, one cutting step can remove all the materials present. The key limitation of the procedure is its cutting speed. Designs featuring rows of bimorphs typically took more than an hour to ablate, meaning that it was necessary to make each prototype in turn, test it, and refine the design before re-ablating. It would be preferable to make many prototypes at once, varying key physical dimensions: any individual testing session would become more productive. This is one reason why ps- or fs-pulse systems should be investigated further: the Lumera Laser ps system, which was studied briefly, can remove material 1000 times faster than a typical ns system.

A reliable way of extracting Young's modulus of thin films has still to be conclusively demonstrated — uncertainties in extracted moduli remain at about 15% — but the work done to study the effects of noise in scanning profilometer data has given a clear understanding of the challenges that we face. Work can now progress apace on improving the two extraction algorithms identified as promising. In the process of designing bimorph microclips, it has become clear that Young's modulus plays only a small role in determining the performance of the devices. The large tolerances of the widths of the components to be held mean that no one design can be conceived so precisely as to offer a 'perfect' holding force. Knowing Young's modulus to within a few percent is of limited use in such a project; the real value of such characterisation work will probably be in designing sensors.

Individual 375μm-long U-shaped thin-film metal-on-SiN actuators have been demonstrated offering curvatures of order 500 $rad.m^{-1}$ for input powers less than 1W. The next stage will be to combine that electrothermal actuation with the large elastic deflections needed to operate the beams as clips for MOEMS packaging. Where film thicknesses are of order 2μm, the bending stresses that would be induced in the existing design have been found by simulation to be ten times the breaking stresses of SiN or the candidate metals. This result indicates that using materials with larger σ_f^3/E^2, such as elastomers, may be fruitful. Alternatively, the work presented here on deep-etched bulk silicon bistable mechanisms, or that on inflatable microclips, could be pursued.

References

[Analog] Moore, DF; reported conversation with staff of Analog Devices, Cambridge, MA.

[Ashby] Ashby, MF; Materials Selection in Mechanical Design; first edition; Pergamon, 1992

[Ashwell] Ashwell, DG; *J. Royal Aeronautical Society* **54 (**1950) pp708–715

[Ayón] Ayón, AA *et al.*; *J. Electrochemical Society* **146** 1 (1999) pp339–349

[Baker] Baker, SP *et al.*; *J.Mater. Res.* **9** 12 (1994) p3137

[Bishop] Bishop, DJ *et al.*; *IEEE Communications Magazine* **40** 3 (2002) pp75–79

[Bostock] Bostock, RM *et al.*; *J. Micromech. Microeng.* **8** (1998) pp343–360

[Boyle] Boyle, P *et al.*; *Proc. IEEE Electronic Components and Tech. Conference* (2002)

[Boyle1] Boyle, P; *Bent Beam Actuators*; internal report, CUED, December 2003

[Chen] Chen, W-C *et al.*; *Sensors and Actuators A* **103** (2003) pp48–58

[Chu] Chu, PB *et al.*; *Proc. IEEE Tenth Annual Int'l Workshop on MEMS* (1997) pp350–355

[Conradie] Conradie, EH; PhD thesis, CUED, 2002

[Zou] Zou, J *et al.*; *J. MEMS* **8** 4 (1999) pp506–513

[Culpepper] MIT News office; *MIT's Hexflex manipulates the nanoscopic*, 30 September 2003

[Dektak] www.veeco.com

[Denhoff] Denhoff, MW; *J. Micromech. Microeng.* **13** (2003) pp686–692

[Dong] Dong, Y *et al.*; *J. Micromech. Microeng.* **13** (2003) pp680–685

[Enzler] Enzler, A *et al.*; *Micrometer accurate, passive, linear positioning device with large displacement using DRIE structured silicon*; *Proc. Micro and Nano Engineering 2003*, Cambridge, 22–25 Sept. 2003

[Etalon] www.ealingcatalog.com

[Gambling] Gambling, WA *et al.*; *Elect. Lett.* **14** (1978) pp54–55

[Gaspar] Gaspar, J *et al.*; *J. Non-Crystalline Solids* **299–302** (2002) pp1224–1228

[Geisberger] Geisberger, AA *et al.*; *J. MEMS* **12** 4 (2003) pp513ff

[Han] Han, LH *et al.*; *Optimal Design of Thermally Actuated Multilayer Cantilever Microactuators*; presentation, CUED

[He] He, JH; second year PhD report, CUED, September 2003

[He1] He, JH; private communication, May 2004.

[Hogan] Hogan, M *et al.*; *Appl. Phys. Lett.* **53** 10 (1998) pp831–833

[Holmes] Holmes, AS; *Proc. SPIE* **4426** (2002) pp203–9

[Hopcroft] Hopcroft, MA; MPhil thesis, CUED, October 2002

[Jackson] Jackson, SR *et al.*; *Applied Surface Science* **86** (1995) pp223–227

[Jensen] Jensen, BD *et al.*; *Proc. 2001 ASME Int'l Mech. Eng. Congress and Exposition*

[Jones] Ashby, MF & Jones, DRH; Engineering Materials 2; second edition; Butterworth Heinemann, 1998

[Kiesewetter] Kiesewetter, L *et al.*; *Sensors and Actuators A* **35** (1992) pp153–159

[Kubota] Kubota, K *et al.*; *Jpn. J. Appl. Phys.* **42** (2003) pp4079–4083

[Lumera] www.lumera-laser.com

[Madou] Madou, MJ: Fundamentals of Microfabrication; CRC Press, 2002

[Meijer] Meijer, J *et al.*; *Annals of the CIRP* **51** (2002) pp 531–550

[Menčík] Menčík, J *et al.*; *J. Mater. Res.* **14** 5 (1999) pp2151ff

[Mickelson] AR Mickelson *et al*, Optoelectronic Packaging; Wiley, 1997

[Moore1] Moore, DF *et al.*; *Proc. SPIE* **4941** (2002) pp140–147

[Moore2] Moore, DF *et al.*; *MEMS technology for silicon opto-hybrids*; case for support from EPSRC, 2000

[NewWave] www.new-wave.com

[Oshima] Oshima, S *et al.*; *Electrical microconnector using micromachined cantilevers for 3D clip level assembly*; downloaded from world-wide web 28 February 2002

[Osterberg] Osterberg, PM *et al.*; *J. MEMS* **6** 2 (1997) pp107ff

[Qinetiq] Private conversation with Mark McNie from Qinetiq, March 2004.

[Que] Que, P *et al.*; *J. MEMS* **10** 2 (2001) pp247ff

[Riley] Riley *et al.*; Mechanics of Materials; Wiley. pp514ff

[Rogers] Rogers, JW *et al.*; *J. MEMS* **10** 2 (2001) pp280–285

[Sandia] mems.sandia.gov

[Schmid] Schmid, P *et al.*; *Diamond and Related Materials* **12** (2003) pp418–421

[Sharpe] Sharpe, WN *et al.*; *J. MEMS* **6** 3 (1997) pp193ff

[Silverstein] Silverstein, MS *et al.*; *J. Vac. Sci. Technol. B* **16** 6 (1998) pp2957–2967

[Singh] Singh, RK *et al.*; *Physical Review B* **41** 13 pp8843–8859

[Syms] Syms, RRA; *J. Micromech. Microeng.* **12** (2002) pp211–218

[Syms1] Syms, RRA *et al.*; *Sensors and Actuators* **2839** (2000) pp1–11

[Tabata] Tabata, O *et al.*; *Sensors and Actuators* **20** (1989) pp135–141.

[Tai] Tai, Y-C; *IEEE Conf: An Investigation of Micro Structures, Sensors, Actuators, Machines and Robot*; (1990) pp147–152

[Timoshenko] Timoshenko, S; J.O.S.A & R.S.I **11** (1925) p235

[Walker] Walker, SJ *et al.*; *Optics and MEMS*; publication NRL/MR/6636–99–7975 of Naval Research Laboratory, USA (1999)

[Weihs] Weihs, TP *et al.*; *Mat. Res. Soc. Symp. Proc.* **130** (1989)

[Yang] Yang, H *et al.*; *J. Micromech. Microeng.* **14** (2004) pp277–282

[Zhang] Zhang, Y *et al.*; *J. MEMS* **8** 1 (1999) pp43ff